science.sciencemag.org/cgi/content/full/science.abc3557/DC1

Supplementary Materials for

Bright carbonate veins on asteroid (101955) Bennu: Implications for aqueous alteration history

H. H. Kaplan*, D. S. Lauretta, A. A. Simon, V. E. Hamilton, D. N. DellaGiustina, D. R. Golish, D. C. Reuter, C. A. Bennett, K. N. Burke, H. Campins, H. C. Connolly Jr. , J. P. Dworkin, J. P. Emery, D. P. Glavin, T. D. Glotch, R. Hanna, K. Ishimaru, E. R. Jawin, T. J. McCoy, N. Porter, S. A. Sandford, S. Ferrone, B. E. Clark, J.-Y. Li, X.-D. Zou, M. G. Daly, O. S. Barnouin, J. A. Seabrook, H. L. Enos

*Corresponding author. Email: hannah.kaplan@nasa.gov

Published 8 October 2020 on *Science* First Release
DOI: 10.1126/science.abc3557

This PDF file includes:

Other Supplementary Materials for this manuscript include the following:
(available at science.sciencemag.org/cgi/content/full/science.abc3557/DC1)

Data S1 (.csv)

Materials and Methods

OVIRS Spectral Data Processing

We used OVIRS spectra collected during the sample site Reconnaissance flyovers that occurred between 5 and 27 October 2019 (Recon A). During this mission phase, the spacecraft scanned four regions of interest (potential sample sites) from 1 to 1.3 km range to surface to collect data with spatial resolution of ~4 to 5 m cross-track and ~7 to 10 m along-track.

Each OVIRS spectrum was radiometrically calibrated using the standard pipeline process, and this radiance data was resampled to a common wavelength axis (*100*). We subtracted a thermal tail from the radiance by fitting a blackbody model with a single temperature and emissivity to the data. We divided the radiance spectra by range adjusted solar flux to produce *I/F* or reflectance spectra (fig. S2). We used a boxcar function over 12 channels to detect and remove noise spikes at this step. As in (*18*), we obtained continuum-removed spectra by fitting a quadratic function at 2.95, 3.1, and 3.6 μm and dividing this continuum from the spectrum. All OVIRS spectra and laboratory spectra were continuum-removed in the same way to ensure comparability. Solid-line OVIRS spectra shown in Figures 1 and 6 were smoothed with a 3σ Gaussian kernel.

Spectral Identification and Mapping

We employed multiple methods for characterizing the 3.4-μm region in OVIRS spectra. These methods were applied to continuum-removed and boxcar-smoothed spectra, with a window of 9 channels. Band depths were calculated on these spectra as the distance from the continuum to the reflectance value at the wavelength of interest (e.g., 3.47 μm). Absorption area between 3.2 and 3.6 μm ("band area") diagnostic of carbonates and/or organics was calculated on continuum-removed *I/F* spectra. Band minima were found in this spectral region with a function that finds all local minima by comparison of neighboring values. Spectra with the strongest band minimum at 3.41 to 3.42 μm were removed as this indicates a strong feature associated with aliphatic organics (e.g., figs. S1 and S7). Other band minima were recorded and then visually inspected to ensure that they were associated with one of the two minima in the carbonate 3.4-μm region.

We used a set of laboratory spectra with features at 3.4 μm to find the closest spectral matches to Bennu and distinguish the sources of the 3.4-μm feature observed in OVIRS data. Laboratory spectra of the carbonate minerals calcite (61), siderite (56), magnesite (34), dolomite (39), and natrite (3) were obtained from the Brown University Reflectance Experiment Laboratory (RELAB) (*101*) and the United States Geological Survey (USGS) spectral library version 7 (*102*). The spectrum identifiers are given in table S1. The breunnerite diffuse reflectance spectrum was acquired on a Nicolet 6700 FTIR at Stony Brook University using a Nicolet SmartDiffuse reflectance accessory, a DTGS detector, and a KBr beamsplitter. A set of 23 meteorite insoluble organic matter (IOM) spectra were used to match the organic component on Bennu (*23*), as were four organic endmember spectra previously used to analyze the organics on (24) Themis (*22*) (fig. S8).

The laboratory spectra were downsampled to OVIRS wavelengths and continuum-removed with the same method as used for the OVIRS spectra. OVIRS and laboratory continuum-removed data were normalized between 0 and 1 in the 3.4-μm region; this step removed the influence of band

depth so that the quantitative comparison assessed band shapes only (see fig. S1). Each OVIRS spectrum was compared at every channel to each of the laboratory spectral endmembers. We used a chi-square goodness of fit statistic to assess how well each laboratory spectrum's shape matches the OVIRS observation spectral shape and chose the endmember that minimizes chi-square (fig. S9 for examples). We find that chi-square values < 2 provide credible matches to the OVIRS data (Fig. 2) and used only these spectra in our further analyses. In this way, we isolated OVIRS spectral sets corresponding to the various carbonate phases and removed spectra that are either associated with organics or have a complex or noisy 3.2–3.6 μm region that is not strongly associated with either carbonate or organic spectra. We further limited our mapping (Fig. 4) to chi-square < 1 to view the spatial distribution and geologic associations of only the closest matches for carbonate detection (table S2).

A second characterization of the 3.4-μm region was done with a visual inspection of each Recon A spectrum from the Nightingale site. Both the unsmoothed and smoothed data were used to identify features. Spectra were removed if they had the strongest feature at 3.42 μm that indicates the presence of organics. The spectrum was designated a calcite if it had absorptions at ~3.33 to 3.34 μm and ~3.47 to 3.48 μm. The spectrum was designated a dolomite/breunnerite if it had absorption features at ~3.28 to 3.29 μm and ~3.43 and 3.46 μm. The spectrum was designated a magnesite if it had absorption features at ~3.26 to 3.28 μm and ~3.42 to 3.45 μm. Lack of one or both features at these absorption features at strengths greater than the noise means the spectrum was not designated a carbonate. Although this method is qualitative, prone to human bias, and a highly supervised form of classification, the results are nearly identical to the goodness of fit classification in terms of the number of acceptable carbonate matches and the percentage of spots corresponding to calcite. We report the chi-square goodness of fit results in the main text and figures, which results in a higher percentage of spots recorded as magnesite than the supervised classification.

Linear Mixture Modeling

We used spectral modeling to assess the abundance or fraction of carbonate within the OVIRS field of view (FOV). We chose to use a linear mixture model because, at >1 cm thick, the veins and bright features are optically separate from the surrounding host rock and the dark boulders, which means that linear, or areal, mixing (as opposed to nonlinear or intimate mixing) is appropriate for this case (*103, 104*).Therefore, we treated each OVIRS spectrum as a linear combination of "carbonate-poor" Bennu (i.e., an OVIRS spectrum that has minimal evidence of carbonate) and a carbonate laboratory spectrum (fig. S7). We used OVIRS data photometrically corrected to reflectance factor (REFF) with 30° incidence, 0° phase, and 30° emission angles to match the laboratory reflectance measurements.

We chose this approach over the Hapke radiative transfer model (*105*), another spectral modeling method which was previously used to estimate carbonate abundances on Ceres (*26*). One advantage of the Hapke model is the ability to derive grain size and abundances for all surface components, whereas the linear mixing model is dependent on the grain size of the spectral endmember. However, we were not able to obtain a satisfactory set of spectral endmembers for each component on the surface measured under appropriate conditions. In addition, the scattering properties of Bennu's surface are still unconstrained. Previous applications of the Hapke modeling approach to spectra of Ceres, another low-albedo asteroid, required a high abundance

of dark material to model the spectra (e.g., *22*), making it difficult to distinctly estimate carbonate abundances. These factors all lead to large uncertainties on abundances obtained from this approach, hence our choice of the linear mixture model.

The linear mixture modeling approach also comes with some caveats. First, the model makes an intrinsic assumption about particle size based on the selected endmember spectra. In this case, the model assumes that the carbonate particle size is equivalent to the particle size of the laboratory spectra and that the "carbonate-poor" Bennu particle size is the same as in the OVIRS endmember spectra we have chosen. In addition, because the bright features have albedos of 10% to at least 19%, but many carbonates have albedos of ~80% or greater, there is likely a darkening agent mixed into the carbonate veins. This darkening of the carbonates is a separate mixing problem. To deal with this, we chose a "dark" carbonate spectrum and prioritized inclusion of carbonates of varying albedos as endmembers in the model, rather than a full range of particle sizes (fig. S7). Finally, most of Bennu has a 3.4-μm feature, so it is difficult to find a truly carbonate- or organic-free region. For this reason, the abundances we present may be underestimated. Because of these caveats, the model results come with large uncertainties, and we use them to understand the order of magnitude of carbonate necessary to explain the signatures we see, rather than as a precise estimate of abundance.

We find that <1% carbonate is needed to match features at 3.2–3.6, 2.35, and 2.55 μm in the OVIRS spectrum (fig. S7). As expected, the model results depend primarily on the overall albedo of the endmember carbonate, and pure, bright calcites can match the OVIRS features with abundances <0.3%. These small (fraction of a percent) estimated values from the linear mixing model are consistent with the veined and mottled rocks as the carbonate hosts because the bright features account for only a fraction of a percentage of each OVIRS spot.

Image Data Processing

Rocks with veins or bright inclusions were detected by manually examining OCAMS PolyCam panchromatic images taken during the 12 April 2019 Detailed Survey–Baseball Diamond Flyby 6 imaging campaign and the 27 October 2019 Recon A hyperbolic flyover of the Nightingale sample site (*106*). The Detailed Survey images have an average pixel scale of 4.57 cm, and the Recon A images have a pixel scale of 1.67 cm.

To measure the dimensions of the bright veins and exposures, PolyCam images were registered to high-resolution tessellated DTMs (5 cm average facet size) produced from OLA data (*107*). In some cases, we looked at images acquired on several days under varying illumination conditions throughout the Detailed Survey and Recon A mission phases to determine vein morphology.

Normal albedo (NA) information for the veins was obtained by identifying the digital number (DN) of the brightest pixel in the region of interest. To calculate the NA for the host rock, we calculated the mean DN over a region of the host rock devoid of shadow and relatively flat, based on the DTM. We then identified a single pixel that had the value closest to the mean. We used the characteristic vein and host rock pixels to determine the photometric observing conditions, based on the facet to which they register in the DTM.

With the pixels of interest identified, the OCAMS images were calibrated into units of reflectance with a 5% absolute radiometric accuracy according to published procedures (*31*). To

calculate normal albedo, the vein and host-rock pixels were photometrically corrected from the measured photometric conditions to *I/F* values at 0° phase angle, 0° emission angle, and 0° incidence angle (0°, 0°, 0°) using the Robotic Lunar Observatory (ROLO) photometric function and published methods (*33*). The photometric correction yields an additional relative uncertainty of 5% in absolute radiometry. Finally, we determined the precision of the NA values by averaging the results from five images obtained under similar observing conditions in Detailed Survey and five additional images from Recon A (table S3). This analysis yielded an absolute precision uncertainty of 1.9% NA for the veins and 0.6% NA for the host rock. We combined the measurement precision, radiometric accuracy, and photometric uncertainty by calculating the square root of the sum of the squares of these three values. Thus, the total uncertainty is 2.2% NA for the vein and 0.8% NA for the host rock (table S3).

Some of the vein pixels had raw DN between 12,000 and 16,383. DN values above 12,000 are within the nonlinear range of the PolyCam detector, and thus their albedo values are likely underestimated.

The timestamps (YYYYMMDD(T)UTC) of the PolyCam images used to determine the NA of boulder VBR-13 are listed in table S3. For the other two boulders on which we performed detailed analyses, we used images with timestamps 20191026T215132S259 (VBR-10, Figure 5) and 20191026T213254S969_pol_iofL2pan (VBR-14, Figure 5).

Digital Terrain Model

All points in the area of interest were extracted from the globally registered model (*108*) and meshed into a surface using the Poisson Reconstruction meshing technique (*109*) to preserve overhangs where supporting data exist. The typical facet size was 5 cm. Figure S10 shows a typical result.

Kinetic Model

We constrain the timescales of calcite vein deposition using a kinetic model (*79*). The rate (*R*) of calcite formation is given by:

$$R = \frac{dm}{dt} = Ak(\Omega_{cal} - 1)^n \quad \text{(S1)}$$

where the variables are defined as:

dm	the amount of calcite precipitate in mmol
dt	the time required to produce dm in hours
A	surface area in cm^2
k	rate constant in mmol cm^{-2} h^{-1}
n	reaction order
Ω_{cal}	saturation state of calcite

Reaction constants and the reaction order were taken from (*110*). Their results yield *n* values from about 1.5 to 2.5 and log *k* (mmol cm^{-2} h^{-1}) values of –4 to –4.8. Their reaction constants are substantially higher than previous studies, suggesting that our derived timescales are lower

limits. We calculated reaction times across a matrix of values using n of 1.5, 2.0, and 2.5, log k of –4, –4.4., and –4.8, and Ω_{cal} of 2, 4, 6, and 8. Ω_{cal} must be >1 for calcite to precipitate. The four saturation values that we chose are consistent with the range of values used in other models (*111*). We estimated the total volume of calcite observed on Bennu using the two endmembers of vein thickness (3 cm and 15 cm) and assuming that they are 100 cm in length and width, yielding volumes of 30,000 cm^3 and 150,000 cm^3, respectively. The shortest timescales for calcite vein deposition arise when the system has a high reaction order (2.5), has a high rate constant (10^{-4}), and is highly saturated (Ω_{cal} = 8). Using these values in the equation above yields dm/dt of 1.30×10^{-2} mmol $hour^{-1}$ cm^{-2}. Under these conditions, the veins precipitate within 7000 years (3 cm thick) to 35,000 years (15 cm thick). The longest timescales are derived in systems with a low rate constant ($10^{-4.8}$) and low saturation (Ω_{cal} = 2). The values result in a dm/dt of 1.58×10^{-5} mmol $hour^{-1}$ cm^{-2}, regardless of reaction order. Under these conditions, the veins would take between 5.8 million years (3 cm thick) and 29.2 million years (15 cm thick) to form. Given this large range of conditions, the timescales of vein formation are uncertain.

Supplementary Text

Considerations for Carbonate Detection with OVIRS and OTES

The OVIRS data have nominal SNR at 3.4 μm of ~50 (*17, 18*). To determine how well feature shapes can be detected and distinguished, we added generated noise profiles to the carbonate and organic laboratory spectra to degrade them to the same SNR as the OVIRS data and then smoothed both datasets. The resulting band shape in both the noise-added carbonate spectra and the OVIRS spectra are nearly identical, and both retain the "doublet" shape characteristic of carbonate after smoothing (fig. S9).

The SNR drops to <25 longwards of 3.7 μm and is 15 at 4 μm, making it difficult detect the carbonate 4-μm band. We find evidence of an absorption feature near 3.98 μm in many OVIRS spectra (fig. S2B). However, because of the lower SNR in this region, the feature strength is similar to or only slightly stronger than the surrounding noise. We do not consider this band in our classification because the SNR makes it difficult to reliably measure the position or depth of the feature. This 4-μm feature does appear to shift by multiple channels from spectrum to spectrum, which is expected given the varying carbon-bearing mineralogy on Bennu. We also find a relationship between 3.47- and 3.98-μm bands in the subset of OVIRS spectra classified as calcites (fig. S2D). The trend line describing the relationship between the two bands matches the laboratory calcite spectra.

We tested our spectral classification method (described above) by finding the best fitting spectral matches to noise-added laboratory spectra. We generated 1000 random noise profiles, added them to each of the laboratory spectra (e.g., the calcites), smoothed the spectra, and then found the best fitting match to the full set of noise-free laboratory spectra using the chi-square statistic. At SNR of 50, we find that the spectral shapes closely reproduce those we see in OVIRS (fig. S11) and that the spectral matching identifies the correct carbonate endmember >95% of the time (table S2). To reduce this uncertainty, we use a maximum acceptable chi-square value less than the maximum chi-square value that produces a correct match. Smoothing data with this SNR can lead band minima positions to shift by a few channels, which may explain small discrepancies between the band minima of laboratory data and OVIRS data in Figure 3.

Detection of spectral features in the thermal infrared (TIR) is limited by the SNR, among other factors (see main text). The OTES SNR varies from ~150 to 1500 across the spectral range (6.25–50 μm, ~1600–200 cm^{-1}) containing three fundamental carbonate features. The SNR is highest (~1200) for the ν_2 fundamental at ~11.3 μm (886 cm^{-1}). However, the total band depth (also known as spectral contrast) of Bennu TIR spectra is much smaller (2%) than the value used for defining OTES performance requirements (5%, *27*), which increases the contribution from random noise. In the laboratory, at OTES ~17 cm^{-1} spectral resolution, a pure, coarse particulate (or solid) carbonate sample having strong absorptions has a ν2 fundamental band at ~11.3 μm (886 cm^{-1}) that is much narrower (~3 vs. ~26 channels) and has lower contrast (~30 to 60%) than the ν3 fundamental at ~6.35 to 6.74 μm (~1500 cm^{-1}). Given these factors, and the very small percentage of carbonate expected on the surface, the 11.3-μm (886-cm^{-1}) feature is not necessarily any more detectable than the deeper and wider band at higher wavenumbers where SNR is lower.

The fractional contribution of carbonate to the measured scene also affects the TIR spectra. The OTES footprint is ~50 m^2 for nadir observations (vs. ~28 m^2 for OVIRS) during Recon A (and increases in area with increasing emission angle), so the area observed is much larger than the area of the presumed carbonates. Mixing of component spectra is linear within the OTES FOV; assuming strong carbonate bands and ideal SNR, we estimate the fraction of the FOV that must be filled to detect spectral features is a few percent, or ~1 to 2 m^2 for a nadir-viewing spectrum. If we assume that the brighter surface features are concentrations of carbonate, none have been observed to be this large (e.g., fig S5), consistent with no detection in the OTES data. These features are a proportionally larger fraction of the OVIRS FOV, and OVIRS's sensitivity to the carbonate is enhanced if carbonate corresponds to the higher-albedo materials. High albedo at visible wavelengths is not necessarily beneficial to detection in the TIR. Finally, band depths in the near-infrared are not always well correlated with the presence and strength of bands in the TIR for a wide variety of conditions in the laboratory (e.g., *112*), where detectability in both regions is affected differently by various chemical and physical properties.

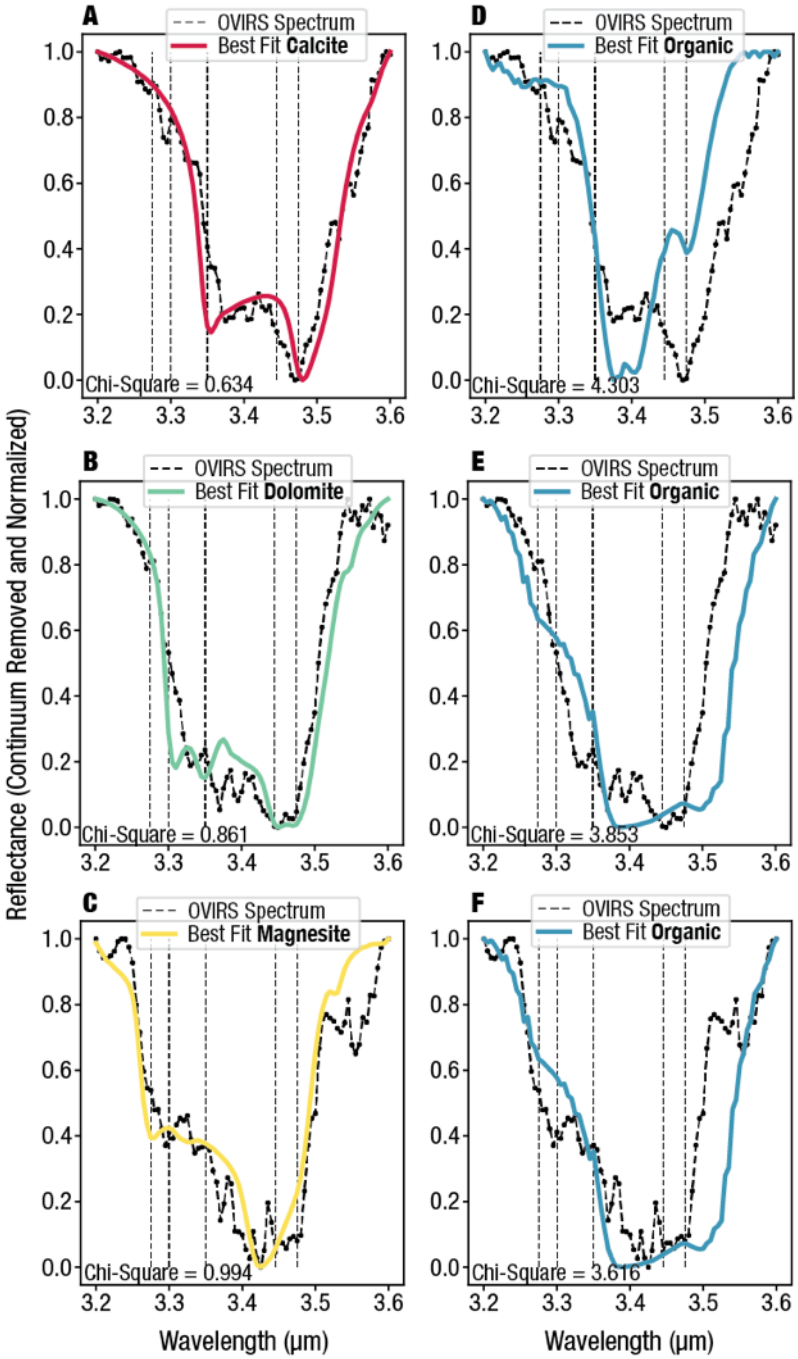

Fig. S1. Best fit comparison between carbonate and organic endmembers. Examples of OVIRS spectra in the 3.2–3. µm region, continuum-removed, smoothed, and normalized, compared to the best match laboratory endmember. (**A** to **C**) Three spectra are shown that are very well matched (chi-square < 1) by carbonates. (**D** to **F**) The same spectra are not well fitted (chi-square > 3.6) by an organic spectrum.

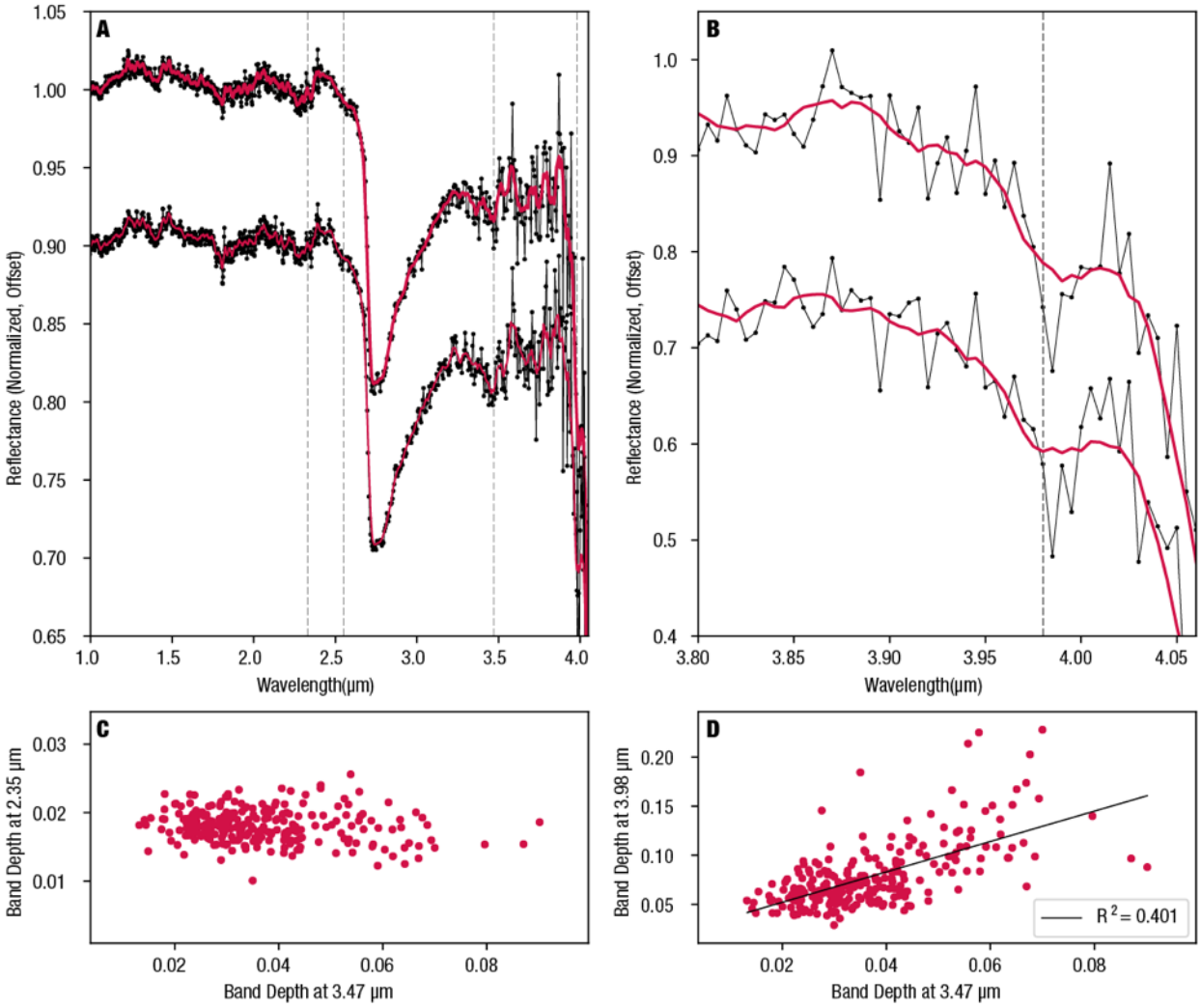

Fig. S2. Carbonate features at multiple wavelengths. (**A**) Two example spectra from Nightingale showing the original (black) and boxcar-smoothed (red) data. Dashed vertical lines indicate potential fundamental and overtone carbonate features at 2.35, 2.55, 3.47, and 3.98 μm; the wavelength region >3.6 μm has lower SNR than the rest of the spectrum. (**B**) The longer wavelength region with a possible band near 3.98 μm. (**C**) The relationship between band depth at 3.47 and 2.35 μm and (**D**) the relationship between band depth at 3.47 and 3.98 μm for a subset of OVIRS spectra that are classified as calcites.

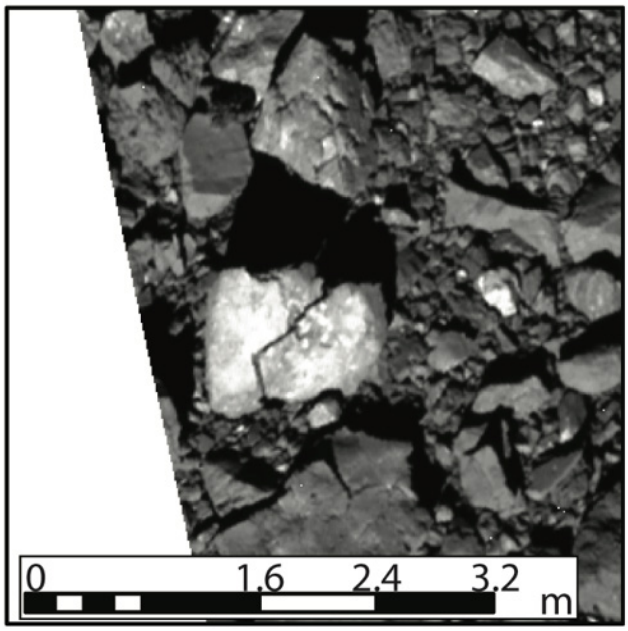

Fig. S3. Another expression of bright, mottled material on Bennu. An example of a boulder where bright material appears to dominate the exposed face. This boulder is located at 54.5°N, 27.8°E.

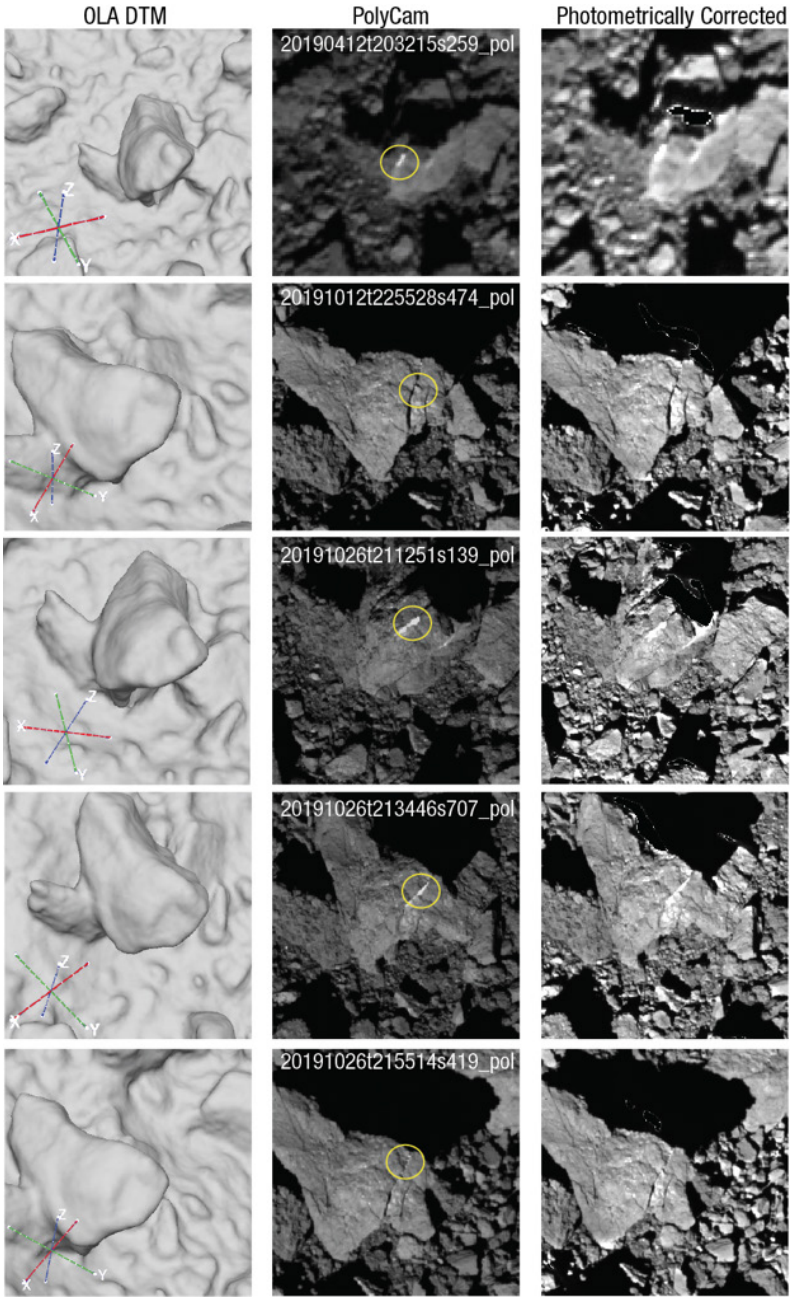

Fig. S4. Multiple observations of a single vein in a boulder. Views of one vein in boulder VBR-13 from multiple observation angles. (**A**) OLA DTMs with orientation information, where *z* is Bennu north-south. (**B**) PolyCam images with the vein marked with a yellow circle. (**C**) The same images as in (**B**), photometrically corrected. The different viewing geometries expose different amounts of the bright material. A description of the pixel size, viewing geometry, and normal albedos of the vein and host rock in each of these images can be found in table S3. The circled vein is ~8 cm wide and 52.5 cm long.

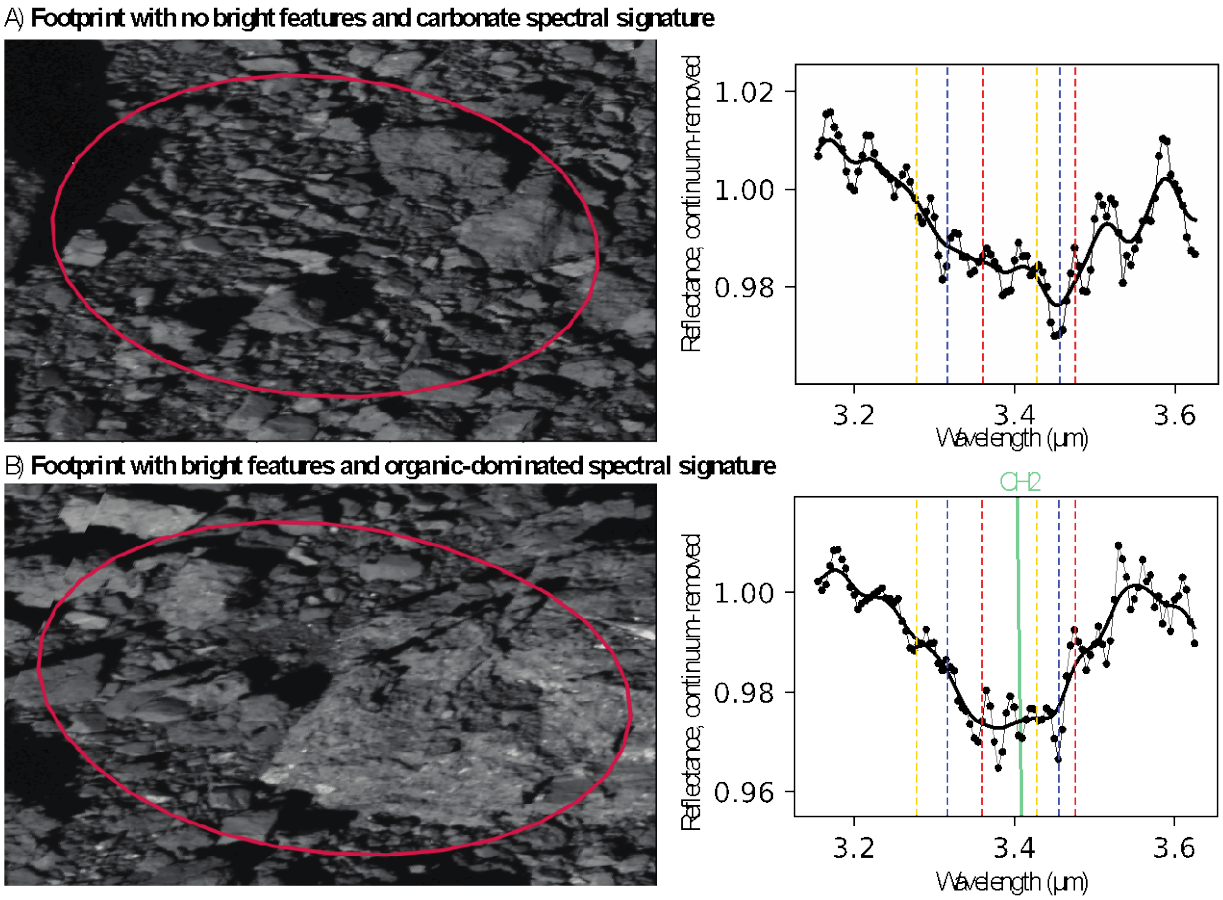

Fig. S5. OVIRS footprints overlaying regions with and without bright features and their spectral signatures. (**A**) An example of an OVIRS footprint that does not appear to cover any boulders with visible bright veins or mottling, but that has a spectral shape in the 3.4-µm region associated with carbonate (specifically, with wavelength positions that are consistent with dolomite/breunnerite). (**B**) An example of an OVIRS footprint that covers a >2-m boulder with bright features, but with a spectral signature that has a rounded shape, rather than having two minima as expected for carbonates. The spectral minimum near 3.41 µm suggests that this spot on the surface is more organic-rich than carbonate-rich. Unsmoothed (black circles) and smoothed (thick black line) spectral data are both shown. Dashed vertical lines indicate the positions of band minima for calcite (red), dolomite/breunnerite (blue), magnesite (yellow), and organic (-CH_2) absorption (green).

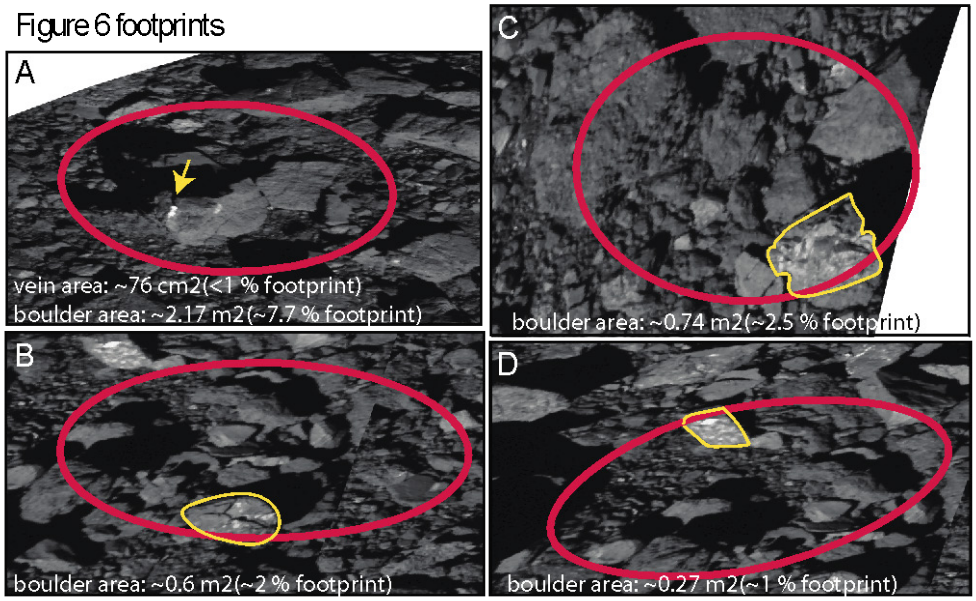

Fig. S6. Estimates of areal exposure of bright features within the OVIRS spectra. These OVIRS footprints in (**A**), (**B**), (**C**), and (**D**) correspond with the panels in order from top to bottom in Fig. 6. Each footprint (red) is 4 m × 4 m and does not account for smear, which would add ~5 m in the along-track (typically, *y*-axis) direction; footprints are visually distorted here by high-latitude projection. Areal percentages of the bright veins or the boulders hosting bright features (indicated in yellow) are given with respect to this assumed 4 m × 9 m footprint.

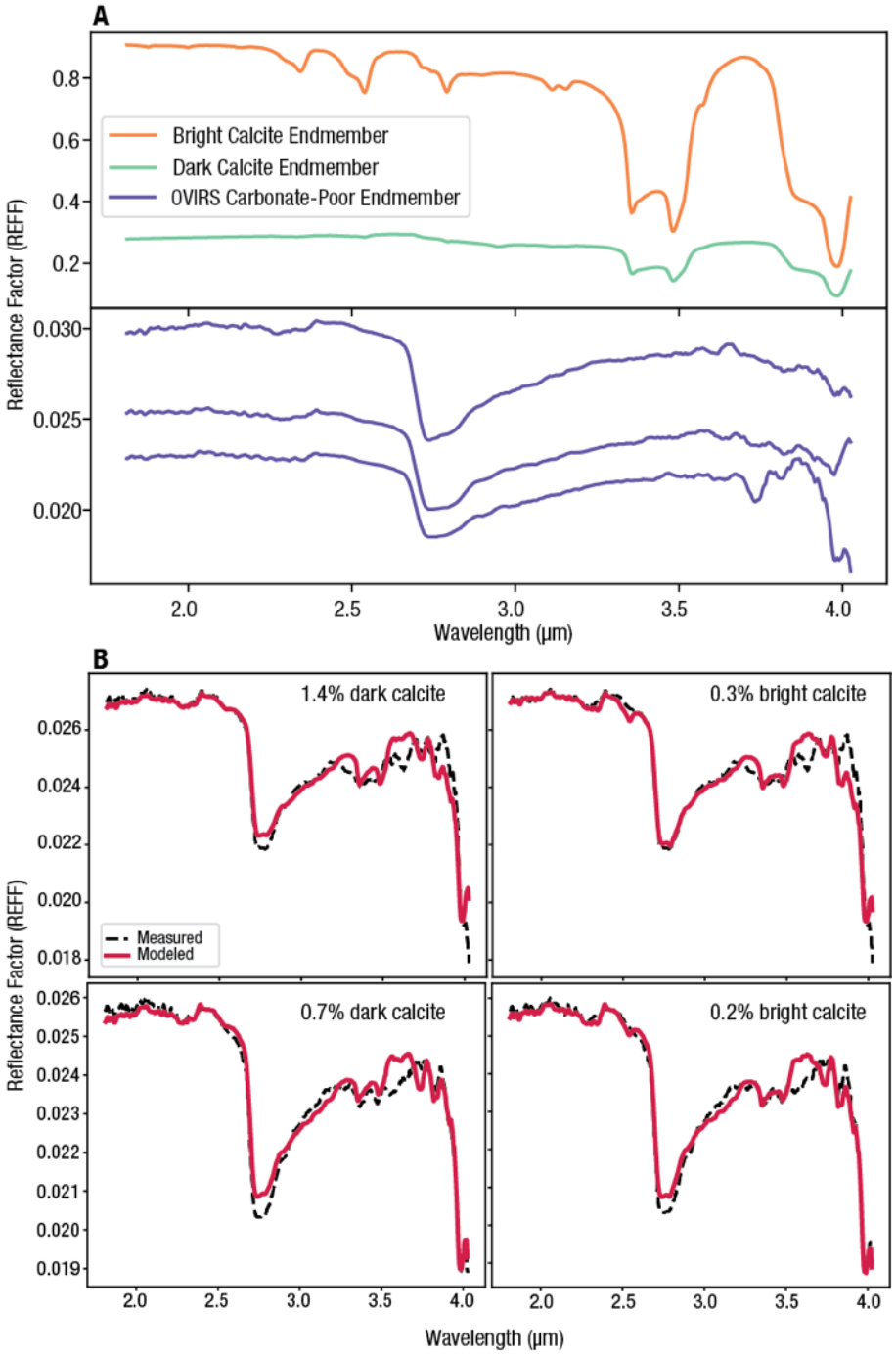

Fig. S7. Additional linear mixing examples using bright and dark calcite endmembers. (**A**) The full set of endmembers used in the linear mixing model including a bright calcite (RELAB: CB-EAC-012-A) and dark calcite (RELAB: CB-EAC-013-B), which has an albedo similar to the bright features on Bennu, and three carbonate-poor OVIRS spectra. (**B**) The best-fitting results and estimated carbonate abundance for two OVIRS spectra with calcite features are shown using bright and dark calcite endmembers. These spectra have been photometrically corrected to reflectance factor (REFF); see text.

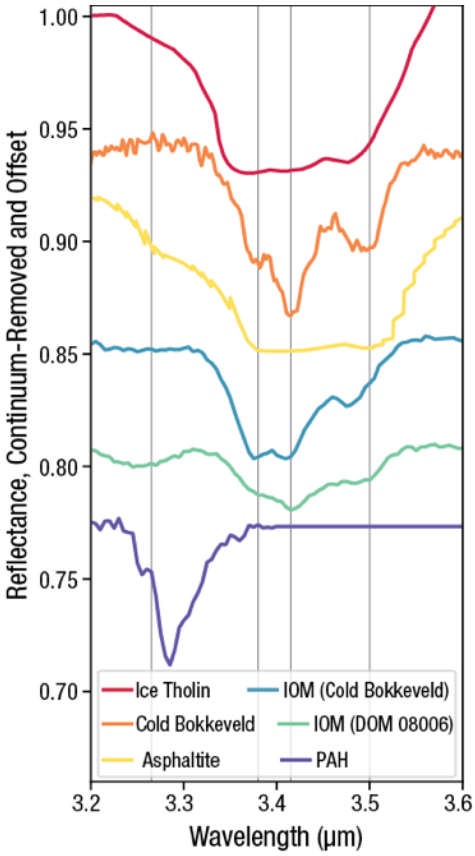

Fig. S8. Organic laboratory endmembers used for classification. The ice tholin, Cold Bokkeveld, aslphaltite, and polycyclic aromatic hydrocarbon (PAH) spectra were compared to (24) Themis organics (*22)*. The two IOM are examples from a full set of 23 spectra (*23*).

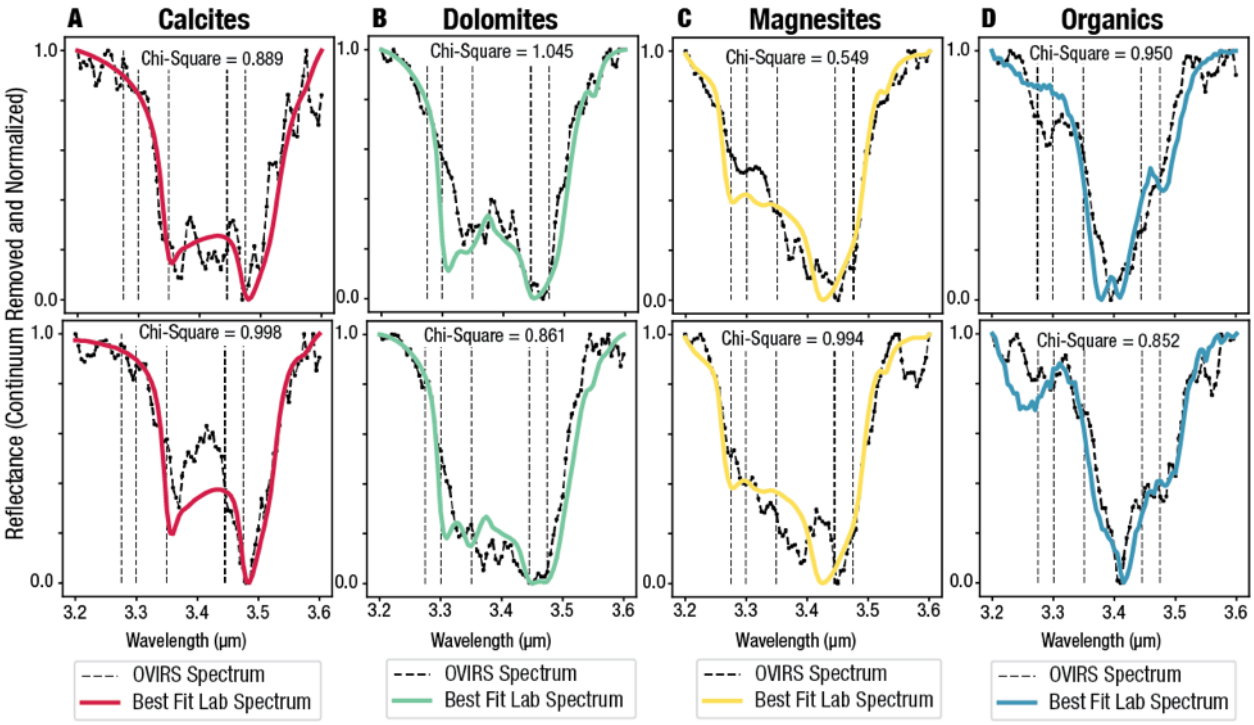

Fig. S9. More examples of OVIRS spectra fit with laboratory endmembers in the region from 3.2 to 3.6 µm. All OVIRS spectra shown were continuum-removed, smoothed, and normalized, compared to the best match laboratory endmember, as shown in Fig. 1A. Chi-square values demonstrate the goodness of fit between the shape of the OVIRS spectrum and laboratory endmember.

Fig. S10. Example OLA data used in this study. A cloud of data points from a single OLA scan over VBR-13.

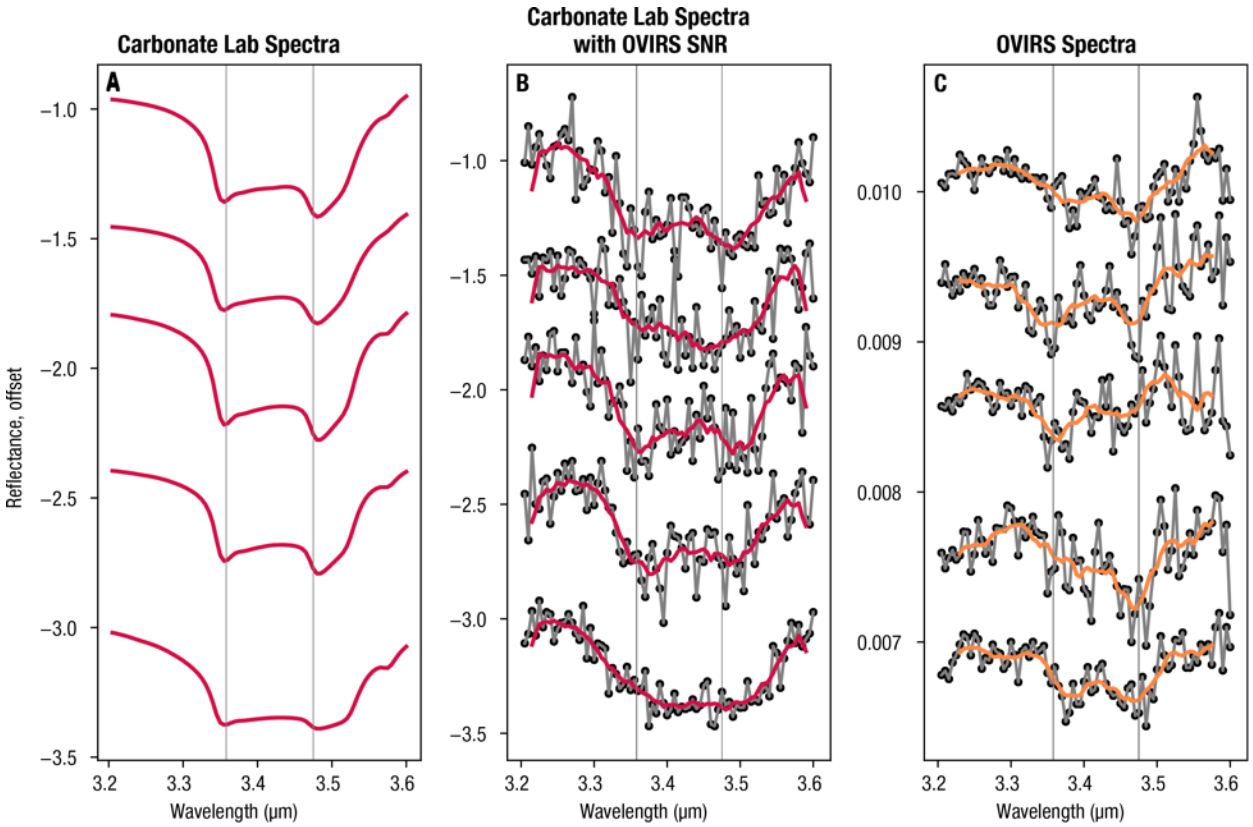

Fig. S11. Degrading laboratory carbonate spectra to OVIRS SNR to compare with observations. (**A**) A set of laboratory calcite spectra with (**B**) noise added to match the OVIRS SNR and then smoothed (red) with the 9-channel boxcar filter to match the OVIRS analyses, compared to (**C**) five OVIRS spectra with their native SNR and smoothed (orange).

Table S1. Laboratory spectra that were used for comparison to Bennu spectra.
Laboratory spectra used in the Figures 1, 2, and 3 obtained from RELAB (*101*) and USGS spectral libraries (*102*).

Carbonate	Sample	Spectral Library	Filename	Figure
Calcite	CAL110 <45 µm	RELAB Spectral Library	CA-EAC-010_CACA10	3
Calcite	CAL110 <45 µm	RELAB Spectral Library	CA-EAC-010_LACA10	3
Calcite	CAL110 <45 µm	RELAB Spectral Library	CA-EAC-010_M1CA10	3
Calcite	CRB109 <45 µm	RELAB Spectral Library	CB-EAC-009-A_LACB09A	3
Calcite	CRB109 45-90 µm	RELAB Spectral Library	CB-EAC-009-B_LACB09B	3
Calcite	CRB110 <45 µm	RELAB Spectral Library	CB-EAC-010-A_LACB10A	3
Calcite	CRB111 <45 µm	RELAB Spectral Library	CB-EAC-011-A_LACB11A	3
Calcite	CRB112 <45 µm	RELAB Spectral Library	CB-EAC-012-A_LACB12A	3
Calcite	CRB112 45-90 µm	RELAB Spectral Library	CB-EAC-012-B_LACB12B	3
Calcite	CRB113 <45 µm	RELAB Spectral Library	CB-EAC-013-A_LACB13A	3
Calcite	CRB113 45-90 µm	RELAB Spectral Library	CB-EAC-013-B_LACB13B	3
Calcite	CRB128 <45 µm	RELAB Spectral Library	CB-EAC-063-A_BKR1CB063A	1,3
Calcite	CRB130 <45 µm	RELAB Spectral Library	CB-EAC-064-A_BKR1CB064A	3
Calcite	CRB131 <45 µm	RELAB Spectral Library	CB-EAC-065-A_BKR1CB065A	3
Calcite	CRB800 <45 µm	RELAB Spectral Library	CB-EAC-077-A_BKR1CB077A	3
Calcite	CRB801 <45 µm	RELAB Spectral Library	CB-EAC-078-A_BKR1CB078A	3
Calcite	Monohydrocalcite	RELAB Spectral Library	CB-MSG-099_BIR2CB099	3
Calcite	Calcite	RELAB Spectral Library	CY-PLH-005_C1CY05	3
Calcite	Calcite CO2004	USGS Spectral Library Version 7	Calcite_CO2004_BECKb_AREF	3
Calcite	Calcite GDS304 75-150 µm	USGS Spectral Library Version 7	Calcite_GDS304_75-150um_ASDFRb_AREF	3
Calcite	Calcite HS48	USGS Spectral Library Version 7	Calcite_HS48.3B_BECKa_AREF	3
Calcite	Calcite WS272	USGS Spectral Library Version 7	Calcite_WS272_ASDNGa_AREF	3
Calcite	Calcite WS272	USGS Spectral Library Version 7	Calcite_WS272_BECKa_AREF	3
Calcite	Calcite WS272	USGS Spectral Library Version 7	Calcite_WS272_NIC4aaa_RREF	3
Calcite	PIG004	RELAB Spectral Library	EC-EAC-004_LAEC04	3
Calcite	Calcite	RELAB Spectral Library	GR-CMP-001_CAGR01	3
Calcite	HYD-BLT-1a	RELAB Spectral Library	HM-JFM-001_C1HM01	3
Calcite	Separate 1 from JA #79634	RELAB Spectral Library	JA-CMP-002-A_C1JA02A	3
Calcite	Lane calcite <63	RELAB Spectral Library	JB-JLB-549_BKR1JB549	3
Calcite	Lane calcite 63-90	RELAB Spectral Library	JB-JLB-550_BKR1JB550	3
Calcite	Lane calcite 90-125	RELAB Spectral Library	JB-JLB-551_1101S551	3
Calcite	Lane calcite 125-180	RELAB Spectral Library	JB-JLB-552_1101S552	3
Calcite	Lane calcite 180-250	RELAB Spectral Library	JB-JLB-553_1101S553	3
Calcite	Lane calcite 250-355	RELAB Spectral Library	JB-JLB-554_1101S554	3
Calcite	Lane calcite 355-500	RELAB Spectral Library	JB-JLB-555_1101S555	3
Calcite	Mazada calcite <45 µm	RELAB Spectral Library	JB-JLB-E57-A_BKR1JBE57A	3
Calcite	Mazada calcite 45-75 µm	RELAB Spectral Library	JB-JLB-E57-B_BKR1JBE57B	3
Calcite	Mazada calcite 75-90 µm	RELAB Spectral Library	JB-JLB-E57-C_BKR1JBE57C	3
Calcite	Mazada calcite 90-125 µm	RELAB Spectral Library	JB-JLB-E57-D_BKR1JBE57D	3
Calcite	Mazada calcite 125-250 µm	RELAB Spectral Library	JB-JLB-E57-E_BKR1JBE57E	3
Calcite	Mazada calcite >250 µm	RELAB Spectral Library	JB-JLB-E57-F_BKR1JBE57F	3
Calcite	Big Timber calcite <45 µm	RELAB Spectral Library	JB-JLB-E58-A_BKR1JBE58A	3
Calcite	Big Timber calcite 45-75 µm	RELAB Spectral Library	JB-JLB-E58-B_BKR1JBE58B	3
Calcite	Big Timber calcite 75-90 µm	RELAB Spectral Library	JB-JLB-E58-C_BKR1JBE58C	3
Calcite	Big Timber calcite 90-125 µm	RELAB Spectral Library	JB-JLB-E58-D_BKR1JBE58D	3
Calcite	Big Timber calcite 125-250 µm	RELAB Spectral Library	JB-JLB-E58-E_BKR1JBE58E	3
Calcite	Big Timber calcite >250 µm	RELAB Spectral Library	JB-JLB-E58-F_BKR1JBE58F	3
Calcite	E95-15A	RELAB Spectral Library	MS-REA-037_NCMS37	3
Calcite	1546a	RELAB Spectral Library	OS-SJG-019_C1OS19	3
Calcite	1546b	RELAB Spectral Library	OS-SJG-020_C1OS20	3
Calcite	Calcite 45-125	RELAB Spectral Library	PC-CMP-050_C1PC50	3
Calcite	Red Calcite	RELAB Spectral Library	PC-CMP-055_C1PC55	3
Calcite	Calcite 1557	RELAB Spectral Library	PC-SJG-002_C1PC02	3
Calcite	Calcite 1556	RELAB Spectral Library	PC-SJG-005_C1PC05	3
Calcite	Calcite 1558 b	RELAB Spectral Library	PC-SJG-006_C1PC06	3

Carbonate	Sample	Spectral Library	Filename	Figure
Calcite	Calcite 1566	RELAB Spectral Library	PC-SJG-008_C1PC08	3
Calcite	Calcite 6506	RELAB Spectral Library	PC-SJG-009_C1PC09	3
Calcite	Calcite 1525	RELAB Spectral Library	PC-SJG-010_C1PC10	3
Calcite	Calcite 1519	RELAB Spectral Library	PC-SJG-011_C1PC11	3
Calcite	Calcite 1529	RELAB Spectral Library	PC-SJG-012_C1PC12	3
Calcite	Calcite 1531	RELAB Spectral Library	PC-SJG-013_C1PC13	3
Dolomite	CRB103 <45 µm	RELAB Spectral Library	CB-EAC-003-A_LACB03A	3
Dolomite	CRB103 45-90 µm	RELAB Spectral Library	CB-EAC-003-B_LACB03B	3
Dolomite	CRB117 <45 µm	RELAB Spectral Library	CB-EAC-017-A_BKR1CB017A	3
Dolomite	Dolomite	RELAB Spectral Library	CC-JFM-005-B_F1CC05B	3
Dolomite	Dolomite	RELAB Spectral Library	CY-PLH-007_C1CY07	3
Dolomite	Dolomite COD2005	USGS Spectral Library Version 7	Dolomite_COD2005_BECKb_AREF	3
Dolomite	Dolomite HS102	USGS Spectral Library Version 7	Dolomite_HS102.1B_ASDNGb_AREF	3
Dolomite	Dolomite HS102	USGS Spectral Library Version 7	Dolomite_HS102.3B_ASDNGb_AREF	3
Dolomite	Dolomite HS102	USGS Spectral Library Version 7	Dolomite_HS102.3B_BECKb_AREF	3
Dolomite	Dolomite HS102	USGS Spectral Library Version 7	Dolomite_HS102.3B_NIC4bbb_RREF	3
Dolomite	Dolomite HS102	USGS Spectral Library Version 7	Dolomite_HS102.4B_ASDNGb_AREF	3
Dolomite	Dolomite ML97-3 Ferroan	USGS Spectral Library Version 7	Dolomite_ML97-3_Ferroan_ASDFRb_AREF	3
Dolomite	Little Red Hill carbonate rock <45 µm	RELAB Spectral Library	JB-JLB-608-J_BKR1JB608J	3
Dolomite	Little Red Hill carbonate rock 45-75 µm	RELAB Spectral Library	JB-JLB-608-K_BKR1JB608K	3
Dolomite	Little Red Hill carbonate rock 75-125 µm	RELAB Spectral Library	JB-JLB-608-L_BKR1JB608L	3
Dolomite	Little Red Hill carbonate rock >125 µm	RELAB Spectral Library	JB-JLB-608-M_BKR1JB608M	3
Dolomite	Fe dolomite <125 µm	RELAB Spectral Library	JB-JLB-779_BKR1JB779	3
Dolomite	Selasvann dolomite <45 µm	RELAB Spectral Library	JB-JLB-E61-A_BKR1JBE61A	3
Dolomite	Selasvann dolomite 45-75 µm	RELAB Spectral Library	JB-JLB-E61-B_BKR1JBE61B	3
Dolomite	Selasvann dolomite 75-90 µm	RELAB Spectral Library	JB-JLB-E61-C_BKR1JBE61C	3
Dolomite	Selasvann dolomite 90-125 µm	RELAB Spectral Library	JB-JLB-E61-D_BKR1JBE61D	3
Dolomite	Selasvann dolomite 125-250 µm	RELAB Spectral Library	JB-JLB-E61-E_BKR1JBE61E	3
Dolomite	Selasvann dolomite >250 µm	RELAB Spectral Library	JB-JLB-E61-F_BKR1JBE61F	1,3
Dolomite	Dolomite 6524	RELAB Spectral Library	PD-SJG-002_C1PD02	3
Dolomite	Dolomite 6252	RELAB Spectral Library	PD-SJG-003_C1PD03	3
Dolomite	Dolomite 6526	RELAB Spectral Library	PD-SJG-004_C1PD04	3
Dolomite	Dolomite 2501	RELAB Spectral Library	PD-SJG-005_C2PD05	3
Dolomite	6509 Dolomite	RELAB Spectral Library	SH-SJG-006_C1SH06	3
Dolomite	6510b Dolomite	RELAB Spectral Library	SH-SJG-007_C1SH07	3
Dolomite	6508 Dolomite	RELAB Spectral Library	SH-SJG-008_C1SH08	3
Dolomite	6521 Dolomite	RELAB Spectral Library	SH-SJG-077_NASH77	3
Dolomite	6523 Dolomite	RELAB Spectral Library	SH-SJG-078_NASH78	3
Dolomite	6528 Dolomite	RELAB Spectral Library	SH-SJG-079_NASH79	3
Dolomite	6529 Dolomite	RELAB Spectral Library	SH-SJG-080_NASH80	3
Dolomite	6503 Dolomite	RELAB Spectral Library	SH-SJG-085_C1SH85	3
Dolomite	6514 Dolomite	RELAB Spectral Library	SH-SJG-086_C1SH86	3
Dolomite	6515A Dolomite	RELAB Spectral Library	SH-SJG-087_C1SH87	3
Dolomite	5501 Dolomite	RELAB Spectral Library	SH-SJG-090_C1SH90	3
Dolomite	6502 Dolomite	RELAB Spectral Library	SH-SJG-091_C1SH91	3
Magnesite	MGC 45-75 µm	RELAB Spectral Library	BE-BLE-256_CABE256	3
Magnesite	MGC 45-75 µm	RELAB Spectral Library	BE-BLE-256_CBBE256	1,3
Magnesite	MGC 45-75 µm	RELAB Spectral Library	BE-BLE-256_CCBE256	3
Magnesite	MGC 45-75 µm	RELAB Spectral Library	BE-BLE-256_CDBE256	3
Magnesite	MGC 45-75 µm	RELAB Spectral Library	BE-BLE-256_CEBE256	3
Magnesite	MGC 45-75 µm	RELAB Spectral Library	BE-BLE-256_CFBE256	3
Magnesite	MGC 45-75 µm	RELAB Spectral Library	BE-BLE-256_CGBE256	3
Magnesite	MGC 45-75 µm	RELAB Spectral Library	BE-BLE-256_CHBE256	3
Magnesite	MGC 45-75 µm	RELAB Spectral Library	BE-BLE-256_CIBE256	3
Magnesite	MGC 45-75 µm	RELAB Spectral Library	BE-BLE-256_CJBE256	3
Magnesite	MGC 45-75 µm	RELAB Spectral Library	BE-BLE-256_CKBE256	3
Magnesite	MGC 45-75 µm	RELAB Spectral Library	BE-BLE-256_CLBE256	3
Magnesite	MGC 45-75 µm	RELAB Spectral Library	BE-BLE-256_CMBE256	3
Magnesite	MGC 45-75 µm	RELAB Spectral Library	BE-BLE-256_CNBE256	3
Magnesite	MGC 45-75 µm	RELAB Spectral Library	BE-BLE-256_COBE256	3
Magnesite	MGC 45-75 µm	RELAB Spectral Library	BE-BLE-256_CPBE256	3

Carbonate	Sample	Spectral Library	Filename	Figure
Magnesite	MGC 45-75 µm	RELAB Spectral Library	BE-BLE-256_CQBE256	3
Magnesite	Magnesite (CC-06B)	RELAB Spectral Library	BE-JFM-044_BKR1BE044	3
Magnesite	MGC <25 µm	RELAB Spectral Library	BE-JFM-222_BKR1BE222	3
Magnesite	MGC 25-45 µm	RELAB Spectral Library	BE-JFM-223_BKR1BE223	3
Magnesite	MGC 45-63 µm	RELAB Spectral Library	BE-JFM-224_BKR1BE224	3
Magnesite	MGC 63-75 µm	RELAB Spectral Library	BE-JFM-225_BKR1BE225	3
Magnesite	MGC 75-106 µm	RELAB Spectral Library	BE-JFM-226_BKR1BE226	3
Magnesite	MGC 106-125 µm	RELAB Spectral Library	BE-JFM-227_BKR1BE227	3
Magnesite	MGC 125-150 µm	RELAB Spectral Library	BE-JFM-228_BKR1BE228	3
Magnesite	MGC 150-250 µm	RELAB Spectral Library	BE-JFM-229_BKR1BE229	3
Magnesite	MGC 250-500 µm	RELAB Spectral Library	BE-JFM-230_BKR1BE230	3
Magnesite	MGC 45-75 µm	RELAB Spectral Library	BE-JFM-231_BKR1BE231	3
Magnesite	CRB106 <45 µm	RELAB Spectral Library	CB-EAC-006-A_LACB06A	3
Magnesite	CRB106 45-90 µm	RELAB Spectral Library	CB-EAC-006-B_LACB06B	3
Magnesite	CRB114 <45 µm	RELAB Spectral Library	CB-EAC-014-A_BKR1CB014A	3
Magnesite	CRB208 <45 µm	RELAB Spectral Library	CB-EAC-028-A_LACB28A	3
Magnesite	CRB208 45-90 µm	RELAB Spectral Library	CB-EAC-028-B_LACB28B	3
Magnesite	CRB215 <45 µm	RELAB Spectral Library	CB-EAC-035-A_LACB35A	3
Siderite	CRB108 <45 µm	RELAB Spectral Library	CB-EAC-008-A_CACB08	3
Siderite	CRB108 <45 µm	RELAB Spectral Library	CB-EAC-008-A_KACB08A	3
Siderite	CRB108 <45 µm	RELAB Spectral Library	CB-EAC-008-A_LACB08A	3
Siderite	CRB108 45-90 µm	RELAB Spectral Library	CB-EAC-008-B_CBCB08	3
Siderite	CRB108 45-90 µm	RELAB Spectral Library	CB-EAC-008-B_KACB08B	3
Siderite	CRB108 45-90 µm	RELAB Spectral Library	CB-EAC-008-B_LACB08B	3
Siderite	CRB141 <45 µm	RELAB Spectral Library	CB-EAC-067-A_BIR1CB067A	3
Siderite	CRB141 <45 µm	RELAB Spectral Library	CB-EAC-067-A_BKR1CB067A	3
Siderite	CRB141 <45 µm	RELAB Spectral Library	CB-EAC-067-A_CACB67	3
Siderite	CRB143 <45 µm	RELAB Spectral Library	CB-EAC-069-A_BIR1CB069A	3
Siderite	CRB143 <45 µm	RELAB Spectral Library	CB-EAC-069-A_BKR1CB069A	1,3
Siderite	CRB143 <45 µm	RELAB Spectral Library	CB-EAC-069-A_CACB69	3
Siderite	CRB145 <45 µm	RELAB Spectral Library	CB-EAC-071-A_BIR1CB071A	3
Siderite	CRB145 <45 µm	RELAB Spectral Library	CB-EAC-071-A_BKR1CB071A	3
Siderite	CRB145 <45 µm	RELAB Spectral Library	CB-EAC-071-A_CACB71	3
Siderite	CRB148 <45 µm	RELAB Spectral Library	CB-EAC-073-A_BIR1CB073A	3
Siderite	CRB148 <45 µm	RELAB Spectral Library	CB-EAC-073-A_BKR1CB073A	3
Siderite	CRB148 <45 µm	RELAB Spectral Library	CB-EAC-073-A_CACB73	3
Siderite	CRB701 <45 µm	RELAB Spectral Library	CB-EAC-074-A_BIR1CB074A	3
Siderite	CRB701 <45 µm	RELAB Spectral Library	CB-EAC-074-A_BKR1CB074A	3
Siderite	CRB701 <45 µm	RELAB Spectral Library	CB-EAC-074-A_CACB74	3
Siderite	Siderite	RELAB Spectral Library	CC-JFM-007-A_N1CC07A	3
Siderite	Siderite	RELAB Spectral Library	CC-JFM-007-B_CBCC07	3
Siderite	Siderite	RELAB Spectral Library	CC-JFM-007-B_F1CC07B	3
Siderite	Siderite	RELAB Spectral Library	CC-JFM-007-C_N1CC07C	3
Siderite	Siderite	RELAB Spectral Library	CY-PLH-024_C1CY24	3
Siderite	Siderite	RELAB Spectral Library	GR-CMP-003_C1GR03	3
Siderite	Siderite	RELAB Spectral Library	GR-CMP-003_CAGR03	3
Siderite	Siderite	RELAB Spectral Library	GR-CMP-003_NAGR03	3
Siderite	Siderite <45 µm	RELAB Spectral Library	JB-JLB-287_C1JB287	3
Siderite	Chalcosiderite P39	RELAB Spectral Library	JB-JLB-747_BIR1JB747	3
Siderite	Chalcosiderite P39	RELAB Spectral Library	JB-JLB-747_BKR1JB747	3
Siderite	Chalcosiderite P39	RELAB Spectral Library	JB-JLB-747_C1JB747	3
Siderite	Antigonish Co. siderite <45 µm	RELAB Spectral Library	JB-JLB-E62-A_BIR1JBE62A	3
Siderite	Antigonish Co. siderite <45 µm	RELAB Spectral Library	JB-JLB-E62-A_BKR1JBE62A	3
Siderite	Antigonish Co. siderite <45 µm	RELAB Spectral Library	JB-JLB-E62-A_C1JBE62A	3
Siderite	Antigonish Co. siderite 45-75 µm	RELAB Spectral Library	JB-JLB-E62-B_BIR1JBE62B	3
Siderite	Antigonish Co. siderite 45-75 µm	RELAB Spectral Library	JB-JLB-E62-B_BKR1JBE62B	3
Siderite	Antigonish Co. siderite 45-75 µm	RELAB Spectral Library	JB-JLB-E62-B_C1JBE62B	3
Siderite	Antigonish Co. siderite 75-90 µm	RELAB Spectral Library	JB-JLB-E62-C_BIR1JBE62C	3
Siderite	Antigonish Co. siderite 75-90 µm	RELAB Spectral Library	JB-JLB-E62-C_BKR1JBE62C	3
Siderite	Antigonish Co. siderite 75-90 µm	RELAB Spectral Library	JB-JLB-E62-C_C1JBE62C	3
Siderite	Antigonish Co. siderite 90-125 µm	RELAB Spectral Library	JB-JLB-E62-D_BIR1JBE62D	3
Siderite	Antigonish Co. siderite 90-125 µm	RELAB Spectral Library	JB-JLB-E62-D_BKR1JBE62D	3
Siderite	Antigonish Co. siderite >250 µm	RELAB Spectral Library	JB-JLB-E62-F_BIR1JBE62F	3

Carbonate	Sample	Spectral Library	Filename	Figure
Siderite	Antigonish Co. siderite 90-125 µm	RELAB Spectral Library	JB-JLB-E62-D_C1JBE62D	3
Siderite	Antigonish Co. siderite 125-250 µm	RELAB Spectral Library	JB-JLB-E62-E_BIR1JBE62E	3
Siderite	Antigonish Co. siderite 125-250 µm	RELAB Spectral Library	JB-JLB-E62-E_BKR1JBE62E	3
Siderite	Antigonish Co. siderite 125-250 µm	RELAB Spectral Library	JB-JLB-E62-E_C1JBE62E	3
Siderite	Antigonish Co. siderite >250 µm	RELAB Spectral Library	JB-JLB-E62-F_BKR1JBE62F	3
Siderite	Antigonish Co. siderite >250 µm	RELAB Spectral Library	JB-JLB-E62-F_C1JBE62F	3
Siderite	Litchfield Co. siderite <45 µm	RELAB Spectral Library	JB-JLB-E63-A_BIR1JBE63A	3
Siderite	Litchfield Co. siderite <45 µm	RELAB Spectral Library	JB-JLB-E63-A_BKR1JBE63A	3
Siderite	Litchfield Co. siderite <45 µm	RELAB Spectral Library	JB-JLB-E63-A_C1JBE63A	3
Siderite	Litchfield Co. siderite 45-75 µm	RELAB Spectral Library	JB-JLB-E63-B_BIR1JBE63B	3
Siderite	Litchfield Co. siderite 45-75 µm	RELAB Spectral Library	JB-JLB-E63-B_BKR1JBE63B	3
Natrite	Heated thermonatrite < 45 µm	RELAB Spectral Library	CB-EAC-033-C LACB33C	
Natrite	Heated thermonatrite < 45 µm	RELAB Spectral Library	CB-EAC-033-D LACB33D	
Natrite	Sideronatrite 115164 <45 µm	RELAB Spectral Library	JB-JLB-A72 BKR1JBA72	

Table S2. Detection rate with chi-square spectral matching. Each laboratory spectrum has 1000 OVIRS noise profiles added (i.e., 25 calcite laboratory spectra with 1000 noise profiles = 25,000 total test spectra) with the total number of resulting spectra listed in parentheses after the endmember. Detection rate refers to the number of times the noise-added spectrum is correctly identified vs. the total number of tests.

Endmember	**Detection Rate**	**Max Chi-Square**	**Mean Chi-Square**	**Detection Rate for Chi-Square < 1**	**Incorrectly identified as**
Calcite (25000)	99.1%	6.316	0.588	99.7%	Dolomite
Dolomite (15000)	98.8%	3.092	0.539	99.4%	Calcite
Magnesite (18000)	95.8%	6.418	1.361	99.4%	Organic
Organic (IOM) (11000)	89.9%	9.329	1.080	98.8%	Dolomite, Calcite, Magnesite

Table S3. Images analyzed to obtain albedo of vein in VBR-13. (Top) List of images used to analyze vein and boulder albedo for VBR-13; these images are shown in fig. S4. (Bottom) Repeated observations from multiple mission stages (Detailed Survey, Recon A) that cover the same boulder. Similar albedos are derived from the repeat observations despite differences in viewing geometry.

Distinct Observations Provide Independent Measures of Vein Normal Albedo											
Image Timestamp	Pixel Scale	Location of Vein		Geometry of Observations			Brightness of Vein			Brightness of Host Rock	
(YYYYMMDD(T)UTC)	(cm)	Sample	Line	i (°)	e (°)	α (°)	DN*	I/F	NA	DN	NA
Detailed Survey and Recon-A Images Obtained Under a Range of Photometric Conditions											
20190412T203215S259	4.6	593	337	24	34	36	9872	0.058	15%	5452	7.6%
20191012T225528S474	1.6	494	667	63	38	29	12997	0.046	14%	7807	6.2%
20191026T211251S139	1.5	303	426	22	23	30	14526	0.061	14%	7635	7.1%
20191026T213446S707	1.3	441	371	25	8.1	27	14701	0.061	14%	8774	6.5%
20191026T215514S419	2.1	710	467	65	52	22	12291	0.057	14%	8524	7.1%
Repeated Observations Under Similar Imaging Conditions Assess the Precision of the Measurements											
Image Timestamp	Pixel Scale	Location of Vein		Geometry of Observations			Brightness of Vein			Brightness of Host Rock	
(YYYYMMDD(T)UTC)	(cm)	Sample	Line	i (°)	e (°)	α (°)	DN*	I/F	NA	DN	NA
Detailed Survey Images Obtained Under Similar Photometric Conditions											
20190412T202822S680	4.8	850	232	33	36	36	10916	0.067	18%	5242	7.1%
20190412T203210S522	4.5	700	1011	25	31	36	10699	0.065	17%	4941	6.8%
20190412T203215S259	4.6	593	337	24	34	36	9872	0.058	15%	5452	7.6%
20190412T203658S749	4.7	351	329	33	36	37	10859	0.065	18%	5360	7.2%
20190412T204051S197	4.2	72	420	21	22	37	11641	0.070	19%	5503	6.8%
						Average	10797	0.065	17%	5300	7.1%
						Standard Deviation	632	0.004	1.5%	224	0.3%
Recon-A Images Obtained Under Similar Photometric Conditions											
20191026T205806S105	1.8	516	189	36	35	32	15796	0.067	17%	7626	6.3%
20191026T205812S199	1.8	549	896	36	35	32	13820	0.058	15%	7290	6.0%
20191026T211127S786	1.6	912	34	30	29	31	16383	0.069	17%	8208	6.0%
20191026T211134S932	1.6	968	630	30	29	31	14326	0.060	14%	7977	7.1%
20191026T211251S139	1.5	303	426	22	23	30	14526	0.061	14%	7635	7.1%
						Average	14970	0.063	15%	7747	6.5%
						Standard Deviation	1074	0.005	1.2%	354	0.5%
DN* = Digital Number, values >12000 are in the nonlinear regime of the PolyCam detector and therefore are lower-limits that likely underestimate the vein NA							Measurement Precision		1.9%		0.6%
							Radiometric Accuracy		0.8%		0.3%
							Photometric Uncertainty		0.8%		0.3%
							Total Uncertainty		**2.2%**		**0.8%**

Table S4. Carbonaceous chondrite spectra with carbonate features. A list of carbonaceous chondrite spectra, available in the RELAB spectral library (*101*), that have carbonate in the 3.4-μm region as opposed to organics or no feature. A larger set of 490 spectra labeled as carbonaceous chondrites in RELAB were searched to find these spectra.

Spectrum	Sample	Type	Sample Type	Band Depth (3.47 μm) %*
MB-TXH-098_NAMB98	Kaidun	CR2	Particulate	0.39
MP-TXH-013_NCMP13	Y-793321,99	CM2	Particulate	1.82
MP-TXH-063_LAMP63	LEW88001,14	CM2	Particulate	0.53
MP-TXH-064_LAMP64	MAC88101,12	CM2	Particulate	0.85
MP-TXH-114_BKR1MP114	Dhofar 735	CM2	Particulate	1.22
MP-TXH-128_BMR1MP128	Dhofar 225	CM-an	Particulate	0.42
MP-TXH-149_BMRAMP149	Y-791198,101	CM2	Chip	0.27
MP-TXH-153_BMRAMP153	Y-793601,95	CM2	Chip	0.49

*Average band depth at same position for OVIRS Recon A data is 2.4%

Caption for Data S1. Spectral classifications. Comma-separated variable file listing our classifications of the OVIRS spectra, at all locations where the goodness of fit test had chi-square <2. SCLK is the spacecraft clock reading when the spectrum was collected.

References and Notes

1. D. S. Lauretta, S. S. Balram-Knutson, E. Beshore, W. V. Boynton, C. Drouet d'Aubigny, D. N. DellaGiustina, H. L. Enos, D. R. Golish, C. W. Hergenrother, E. S. Howell, C. A. Bennett, E. T. Morton, M. C. Nolan, B. Rizk, H. L. Roper, A. E. Bartels, B. J. Bos, J. P. Dworkin, D. E. Highsmith, D. A. Lorenz, L. F. Lim, R. Mink, M. C. Moreau, J. A. Nuth, D. C. Reuter, A. A. Simon, E. B. Bierhaus, B. H. Bryan, R. Ballouz, O. S. Barnouin, R. P. Binzel, W. F. Bottke, V. E. Hamilton, K. J. Walsh, S. R. Chesley, P. R. Christensen, B. E. Clark, H. C. Connolly, M. K. Crombie, M. G. Daly, J. P. Emery, T. J. McCoy, J. W. McMahon, D. J. Scheeres, S. Messenger, K. Nakamura-Messenger, K. Righter, S. A. Sandford, OSIRIS-REx: Sample Return from Asteroid (101955) Bennu. *Space Sci. Rev.* **212**, 925–984 (2017). doi:10.1007/s11214-017-0405-1

2. B. E. Clark, R. P. Binzel, E. S. Howell, E. A. Cloutis, M. Ockert-Bell, P. Christensen, M. A. Barucci, F. DeMeo, D. S. Lauretta, H. Connolly Jr., A. Soderberg, C. Hergenrother, L. Lim, J. Emery, M. Mueller, Asteroid (101955) 1999 RQ36: Spectroscopy from 0.4 to 2.4μm and meteorite analogs. *Icarus* **216**, 462–475 (2011). doi:10.1016/j.icarus.2011.08.021

3. V. E. Hamilton, A. A. Simon, P. R. Christensen, D. C. Reuter, B. E. Clark, M. A. Barucci, N. E. Bowles, W. V. Boynton, J. R. Brucato, E. A. Cloutis, H. C. Connolly Jr., K. L. D. Hanna, J. P. Emery, H. L. Enos, S. Fornasier, C. W. Haberle, R. D. Hanna, E. S. Howell, H. H. Kaplan, L. P. Keller, C. Lantz, J. Y. Li, L. F. Lim, T. J. McCoy, F. Merlin, M. C. Nolan, A. Praet, B. Rozitis, S. A. Sandford, D. L. Schrader, C. A. Thomas, X. D. Zou, D. S. Lauretta; OSIRIS-REx Team, Evidence for widespread hydrated minerals on asteroid (101955) Bennu. *Nat. Astron.* **3**, 332–340 (2019). doi:10.1038/s41550-019-0722-2 Medline

4. D. S. Lauretta, D. N. DellaGiustina, C. A. Bennett, D. R. Golish, K. J. Becker, S. S. Balram-Knutson, O. S. Barnouin, T. L. Becker, W. F. Bottke, W. V. Boynton, H. Campins, B. E. Clark, H. C. Connolly Jr., C. Y. Drouet d'Aubigny, J. P. Dworkin, J. P. Emery, H. L. Enos, V. E. Hamilton, C. W. Hergenrother, E. S. Howell, M. R. M. Izawa, H. H. Kaplan, M. C. Nolan, B. Rizk, H. L. Roper, D. J. Scheeres, P. H. Smith, K. J. Walsh, C. W. V. Wolner; OSIRIS-REx Team, The unexpected surface of asteroid (101955) Bennu. *Nature* **568**, 55–60 (2019). doi:10.1038/s41586-019-1033-6 Medline

5. D. DellaGiustina, J. Emery, D. Golish, B. Rozitis, C. Bennett, K. Burke, R.-L. Ballouz, K. Becker, P. Christensen, C. D. d'Aubigny, Properties of rubble-pile asteroid (101955) Bennu from OSIRIS-REx imaging and thermal analysis. *New Astron.* **3**, 341–351 (2019).

6. D. Takir, J. P. Emery, H. Y. Mcsween Jr., C. A. Hibbitts, R. N. Clark, N. Pearson, A. Wang, Nature and degree of aqueous alteration in CM and CI carbonaceous chondrites. *Meteorit. Planet. Sci.* **48**, 1618–1637 (2013). doi:10.1111/maps.12171

7. A. Ghosh, S. J. Weidenschilling, H. Y. McSween Jr., A. E. Rubin, in *Meteorites and the Early Solar System II* (Univ. of Arizona Press, 2006), pp. 555–566.

8. M. Endress, E. Zinner, A. Bischoff, Early aqueous activity on primitive meteorite parent bodies. *Nature* **379**, 701–703 (1996). doi:10.1038/379701a0 Medline

9. O. S. Barnouin, M. G. Daly, E. E. Palmer, R. W. Gaskell, J. R. Weirich, C. L. Johnson, M. M. A. Asad, J. H. Roberts, M. E. Perry, H. C. M. Susorney, R. T. Daly, E. B. Bierhaus, J. A.

Seabrook, R. C. Espiritu, A. H. Nair, L. Nguyen, G. A. Neumann, C. M. Ernst, W. V. Boynton, M. C. Nolan, C. D. Adam, M. C. Moreau, B. Risk, C. D. D'Aubigny, E. R. Jawin, K. J. Walsh, P. Michel, S. R. Schwartz, R.-L. Ballouz, E. M. Mazarico, D. J. Scheeres, J. McMahon, W. Bottke, S. Sugita, N. Hirata, N. Hirata, S. Watanabe, K. N. Burke, D. N. DellaGuistina, C. A. Bennett, D. S. Lauretta; OSIRIS-REx Team., Shape of (101955) Bennu indicative of a rubble pile with internal stiffness. *Nat. Geosci.* **12**, 247–252 (2019). doi:10.1038/s41561-019-0330-x Medline

10. P. Michel, R.-L. Ballouz, O. S. Barnouin, M. Jutzi, K. J. Walsh, B. H. May, C. Manzoni, D. C. Richardson, S. R. Schwartz, S. Sugita, S. Watanabe, H. Miyamoto, M. Hirabayashi, W. F. Bottke, H. C. Connolly, M. Yoshikawa, D. S. Lauretta, Collisional formation of top-shaped asteroids and implications for the origins of Ryugu and Bennu. *Nat. Commun.* **11**, 2655 (2020). doi:10.1038/s41467-020-16433-z Medline

11. K. J. Walsh, M. Delbó, W. F. Bottke, D. Vokrouhlický, D. S. Lauretta, Introducing the Eulalia and new Polana asteroid families: Re-assessing primitive asteroid families in the inner Main Belt. *Icarus* **225**, 283–297 (2013). doi:10.1016/j.icarus.2013.03.005

12. W. R. Van Schmus, J. A. Wood, A chemical-petrologic classification for the chondritic meteorites. *Geochim. Cosmochim. Acta* **31**, 747–765 (1967). doi:10.1016/S0016-7037(67)80030-9

13. H. Y. McSween Jr., S. M. Richardson, The composition of carbonaceous chondrite matrix. *Geochim. Cosmochim. Acta* **41**, 1145–1161 (1977). doi:10.1016/0016-7037(77)90110-7

14. A. E. Rubin, J. M. Trigo-Rodríguez, H. Huber, J. T. Wasson, Progressive aqueous alteration of CM carbonaceous chondrites. *Geochim. Cosmochim. Acta* **71**, 2361–2382 (2007). doi:10.1016/j.gca.2007.02.008

15. M. E. Zolensky, D. W. Mittlefehldt, M. E. Lipschutz, M.-S. Wang, R. N. Clayton, T. K. Mayeda, M. M. Grady, C. Pillinger, D. B, D. B, CM chondrites exhibit the complete petrologic range from type 2 to 1. *Geochim. Cosmochim. Acta* **61**, 5099–5115 (1997). doi:10.1016/S0016-7037(97)00357-8

16. G. W. Kallemeyn, J. T. Wasson, The compositional classification of chondrites: IV. Ungrouped chondritic meteorites and clasts. *Geochim. Cosmochim. Acta* **49**, 261–270 (1985). doi:10.1016/0016-7037(85)90209-1

17. D. C. Reuter, A. A. Simon, J. Hair, A. Lunsford, S. Manthripragada, V. Bly, B. Bos, C. Brambora, E. Caldwell, G. Casto, Z. Dolch, P. Finneran, D. Jennings, M. Jhabvala, E. Matson, M. McLelland, W. Roher, T. Sullivan, E. Weigle, Y. Wen, D. Wilson, D. S. Lauretta, The OSIRIS-REx Visible and InfraRed Spectrometer (OVIRS): Spectral Maps of the Asteroid Bennu. *Space Sci. Rev.* **214**, 54 (2018). doi:10.1007/s11214-018-0482-9

18. A. A. Simon, H. H. Kaplan, V. E. Hamilton, D. S. Lauretta, H. C. Campins, J. P. Emery, M. A. Barucci, D. N. DellaGiustina, D. C. Reuter, S. A. Sandford, D. R. Golish, L. F. Lim, A. Ryan, B. Rozitis, C. A. Bennett, Widespread carbon-bearing materials on near-Earth asteroid (101955) Bennu. *Science* 10.1126/science.abc3522 (2020). doi:10.1126/science.abc3522

19. Materials and methods are available as supplementary materials.

20. M. C. De Sanctis, E. Ammannito, H. Y. McSween, A. Raponi, S. Marchi, F. Capaccioni, M. T. Capria, F. G. Carrozzo, M. Ciarniello, S. Fonte, M. Formisano, A. Frigeri, M. Giardino, A. Longobardo, G. Magni, L. A. McFadden, E. Palomba, C. M. Pieters, F. Tosi, F. Zambon, C. A. Raymond, C. T. Russell, Localized aliphatic organic material on the surface of Ceres. *Science* **355**, 719–722 (2017). doi:10.1126/science.aaj2305 Medline

21. A. Raponi, M. Ciarniello, F. Capaccioni, V. Mennella, G. Filacchione, V. Vinogradoff, O. Poch, P. Beck, E. Quirico, M. C. De Sanctis, L. V. Moroz, D. Kappel, S. Erard, D. Bockelée-Morvan, A. Longobardo, F. Tosi, E. Palomba, J.-P. Combe, B. Rousseau, G. Arnold, R. W. Carlson, A. Pommerol, C. Pilorget, S. Fornasier, G. Bellucci, A. Barucci, F. Mancarella, M. Formisano, G. Rinaldi, I. Istiqomah, C. Leyrat, Infrared detection of aliphatic organics on a cometary nucleus. *New Astron.* **4**, 500–505 (2020).

22. A. S. Rivkin, J. P. Emery, Detection of ice and organics on an asteroidal surface. *Nature* **464**, 1322–1323 (2010). doi:10.1038/nature09028 Medline

23. H. H. Kaplan, R. E. Milliken, C. M. O. Alexander, C. D. K. Herd, Reflectance spectroscopy of insoluble organic matter (IOM) and carbonaceous meteorites. *Meteorit. Planet. Sci.* **54**, 1051–1068 (2019). doi:10.1111/maps.13264

24. M. Endress, A. Bischoff, Carbonates in CI chondrites: Clues to parent body evolution. *Geochim. Cosmochim. Acta* **60**, 489–507 (1996). doi:10.1016/0016-7037(95)00399-1 Medline

25. S. J. Gaffey, Spectral reflectance of carbonate minerals in the visible and near infrared (0.35–2.55 um): Anhydrous carbonate minerals. *J. Geophys. Res.* **92** (B2), 1429 (1987). doi:10.1029/JB092iB02p01429

26. M. C. De Sanctis, A. Raponi, E. Ammannito, M. Ciarniello, M. J. Toplis, H. Y. McSween, J. C. Castillo-Rogez, B. L. Ehlmann, F. G. Carrozzo, S. Marchi, F. Tosi, F. Zambon, F. Capaccioni, M. T. Capria, S. Fonte, M. Formisano, A. Frigeri, M. Giardino, A. Longobardo, G. Magni, E. Palomba, L. A. McFadden, C. M. Pieters, R. Jaumann, P. Schenk, R. Mugnuolo, C. A. Raymond, C. T. Russell, Bright carbonate deposits as evidence of aqueous alteration on (1) Ceres. *Nature* **536**, 54–57 (2016). doi:10.1038/nature18290 Medline

27. P. R. Christensen, V. E. Hamilton, G. L. Mehall, D. Pelham, W. O'Donnell, S. Anwar, H. Bowles, S. Chase, J. Fahlgren, Z. Farkas, T. Fisher, O. James, I. Kubik, I. Lazbin, M. Miner, M. Rassas, L. Schulze, K. Shamordola, T. Tourville, G. West, R. Woodward, D. Lauretta, The OSIRIS-REx Thermal Emission Spectrometer (OTES) Instrument. *Space Sci. Rev.* **214**, 87 (2018). doi:10.1007/s11214-018-0513-6

28. J. L. Bandfield, T. D. Glotch, P. R. Christensen, Spectroscopic identification of carbonate minerals in the martian dust. *Science* **301**, 1084–1087 (2003). doi:10.1126/science.1088054 Medline

29. K. C. Feely, P. R. Christensen, Quantitative compositional analysis using thermal emission spectroscopy: Application to igneous and metamorphic rocks. *J. Geophys. Res. Planets* **104** (E10), 24195–24210 (1999). doi:10.1029/1999JE001034

30. B. Rizk, C. Drouet d'Aubigny, D. Golish, C. Fellows, C. Merrill, P. Smith, M. S. Walker, J. E. Hendershot, J. Hancock, S. H. Bailey, D. N. DellaGiustina, D. S. Lauretta, R. Tanner,

M. Williams, K. Harshman, M. Fitzgibbon, W. Verts, J. Chen, T. Connors, D. Hamara, A. Dowd, A. Lowman, M. Dubin, R. Burt, M. Whiteley, M. Watson, T. McMahon, M. Ward, D. Booher, M. Read, B. Williams, M. Hunten, E. Little, T. Saltzman, D. Alfred, S. O'Dougherty, M. Walthall, K. Kenagy, S. Peterson, B. Crowther, M. L. Perry, C. See, S. Selznick, C. Sauve, M. Beiser, W. Black, R. N. Pfisterer, A. Lancaster, S. Oliver, C. Oquest, D. Crowley, C. Morgan, C. Castle, R. Dominguez, M. Sullivan, OCAMS: The OSIRIS-REx Camera Suite. *Space Sci. Rev.* **214**, 26 (2018). doi:10.1007/s11214-017-0460-7

31. D. R. Golish, C. Drouet d'Aubigny, B. Rizk, D. N. DellaGiustina, P. H. Smith, K. Becker, N. Shultz, T. Stone, M. K. Barker, E. Mazarico, E. Tatsumi, R. W. Gaskell, L. Harrison, C. Merrill, C. Fellows, B. Williams, S. O'Dougherty, M. Whiteley, J. Hancock, B. E. Clark, C. W. Hergenrother, D. S. Lauretta, Ground and In-Flight Calibration of the OSIRIS-REx Camera Suite. *Space Sci. Rev.* **216**, 12 (2020). doi:10.1007/s11214-019-0626-6 Medline

32. O. S. Barnouin, M. G. Daly, E. E. Palmer, C. L. Johnson, R. W. Gaskell, M. Al Asad, E. B. Bierhaus, K. L. Craft, C. M. Ernst, R. C. Espiritu, H. Nair, G. A. Neumann, L. Nguyen, M. C. Nolan, E. Mazarico, M. E. Perry, L. C. Philpott, J. H. Roberts, R. J. Steele, J. Seabrook, H. C. M. Susorney, J. R. Weirich, D. S. Lauretta, Digital terrain mapping by the OSIRIS-REx mission. *Planet. Space Sci.* **180**, 104764 (2020). doi:10.1016/j.pss.2019.104764

33. D. R. Golish, D. N. DellaGiustina, J.-Y. Li, B. E. Clark, X.-D. Zou, P. H. Smith, J. L. Rizos, P. H. Hasselmann, C. A. Bennett, S. Fornasier, R.-L. Ballouz, C. Drouet d'Aubigny, B. Rizk, M. G. Daly, O. S. Barnouin, L. Philpott, M. M. Al Asad, J. A. Seabrook, C. L. Johnson, D. S. Lauretta, Disk-resolved photometric modeling and properties of asteroid (101955) Bennu. *Icarus* 10.1016/j.icarus.2020.113724 (2020). doi:10.1016/j.icarus.2020.113724

34. C. W. Hergenrother, C. K. Maleszewski, M. C. Nolan, J.-Y. Li, C. Y. Drouet d'Aubigny, F. C. Shelly, E. S. Howell, T. R. Kareta, M. R. M. Izawa, M. A. Barucci, E. B. Bierhaus, H. Campins, S. R. Chesley, B. E. Clark, E. J. Christensen, D. N. DellaGiustina, S. Fornasier, D. R. Golish, C. M. Hartzell, B. Rizk, D. J. Scheeres, P. H. Smith, X.-D. Zou, D. S. Lauretta; OSIRIS-REx Team, The operational environment and rotational acceleration of asteroid (101955) Bennu from OSIRIS-REx observations. *Nat. Commun.* **10**, 1291 (2019). doi:10.1038/s41467-019-09213-x Medline

35. T. G. Sharp, P. S. DeCarli, in *Meteorites and the Early Solar System II* (Univ. of Arizona Press, 2006), pp. 653–677.

36. S. Sugita, R. Honda, T. Morota, S. Kameda, H. Sawada, E. Tatsumi, M. Yamada, C. Honda, Y. Yokota, T. Kouyama, N. Sakatani, K. Ogawa, H. Suzuki, T. Okada, N. Namiki, S. Tanaka, Y. Iijima, K. Yoshioka, M. Hayakawa, Y. Cho, M. Matsuoka, N. Hirata, N. Hirata, H. Miyamoto, D. Domingue, M. Hirabayashi, T. Nakamura, T. Hiroi, T. Michikami, P. Michel, R.-L. Ballouz, O. S. Barnouin, C. M. Ernst, S. E. Schröder, H. Kikuchi, R. Hemmi, G. Komatsu, T. Fukuhara, M. Taguchi, T. Arai, H. Senshu, H. Demura, Y. Ogawa, Y. Shimaki, T. Sekiguchi, T. G. Müller, A. Hagermann, T. Mizuno, H. Noda, K. Matsumoto, R. Yamada, Y. Ishihara, H. Ikeda, H. Araki, K. Yamamoto, S. Abe, F. Yoshida, A. Higuchi, S. Sasaki, S. Oshigami, S. Tsuruta, K. Asari, S. Tazawa, M. Shizugami, J. Kimura, T. Otsubo, H. Yabuta, S. Hasegawa, M. Ishiguro, S. Tachibana, E.

Palmer, R. Gaskell, L. Le Corre, R. Jaumann, K. Otto, N. Schmitz, P. A. Abell, M. A. Barucci, M. E. Zolensky, F. Vilas, F. Thuillet, C. Sugimoto, N. Takaki, Y. Suzuki, H. Kamiyoshihara, M. Okada, K. Nagata, M. Fujimoto, M. Yoshikawa, Y. Yamamoto, K. Shirai, R. Noguchi, N. Ogawa, F. Terui, S. Kikuchi, T. Yamaguchi, Y. Oki, Y. Takao, H. Takeuchi, G. Ono, Y. Mimasu, K. Yoshikawa, T. Takahashi, Y. Takei, A. Fujii, C. Hirose, S. Nakazawa, S. Hosoda, O. Mori, T. Shimada, S. Soldini, T. Iwata, M. Abe, H. Yano, R. Tsukizaki, M. Ozaki, K. Nishiyama, T. Saiki, S. Watanabe, Y. Tsuda, The geomorphology, color, and thermal properties of Ryugu: Implications for parent-body processes. *Science* **364**, 252 (2019). doi:10.1126/science.aaw0422 Medline

37. D. N. DellaGiustina *et al*., Variation in color and reflectance of asteroid (101955) Bennu. *Science* (2020). 10.1126/science.abc3660

38. B. Rozitis *et al*., Asteroid (101955) Bennu's Weak Boulders and Thermally Anomalous Equator. *Sci. Adv.* (2020). 10.1126/sciadv.abc3699

39. M. R. Lee, P. Lindgren, M. R. Sofe, Aragonite, breunnerite, calcite and dolomite in the CM carbonaceous chondrites: High fidelity recorders of progressive parent body aqueous alteration. *Geochim. Cosmochim. Acta* **144**, 126–156 (2014). doi:10.1016/j.gca.2014.08.019

40. K. T. Howard, C. M. O. Alexander, D. L. Schrader, K. A. Dyl, Classification of hydrous meteorites (CR, CM and C2 ungrouped) by phyllosilicate fraction: PSD-XRD modal mineralogy and planetesimal environments. *Geochim. Cosmochim. Acta* **149**, 206–222 (2015). doi:10.1016/j.gca.2014.10.025

41. C. M. O. Alexander, R. Bowden, M. L. Fogel, K. T. Howard, Carbonate abundances and isotopic compositions in chondrites. *Meteorit. Planet. Sci.* **50**, 810–833 (2015). doi:10.1111/maps.12410

42. M. R. Lee, P. Lindgren, M. R. Sofe, C. M. O'D Alexander, J. Wang, C. M. O'D Alexander, J. Wang, Extended chronologies of aqueous alteration in the CM2 carbonaceous chondrites: Evidence from carbonates in Queen Alexandra Range 93005. *Geochim. Cosmochim. Acta* **92**, 148–169 (2012). doi:10.1016/j.gca.2012.06.005

43. S. De Leuw, A. E. Rubin, J. T. Wasson, Carbonates in CM chondrites: Complex formational histories and comparison to carbonates in CI chondrites. *Meteorit. Planet. Sci.* **45**, 513–530 (2010). doi:10.1111/j.1945-5100.2010.01037.x

44. L. R. Riciputi, H. Y. McSween Jr., C. A. Johnson, M. Prinz, Minor and trace element concentrations in carbonates of carbonaceous chondrites, and implications for the compositions of coexisting fluids. *Geochim. Cosmochim. Acta* **58**, 1343–1351 (1994). doi:10.1016/0016-7037(94)90386-7

45. J. Alfing, M. Patzek, A. Bischoff, Modal abundances of coarse-grained (>5 μm) components within CI-chondrites and their individual clasts – Mixing of various lithologies on the CI parent body(ies). *Geochemistry* **79**, 125532 (2019). doi:10.1016/j.chemer.2019.08.004

46. K. Fredriksson, J. F. Kerridge, Carbonates and sulfates in CI chondrites: Formation by aqueous activity on the parent body. *Meteoritics* **23**, 35–44 (1988). doi:10.1111/j.1945-5100.1988.tb00894.x Medline

47. C. A. Johnson, M. Prinz, Carbonate compositions in CM and CI chondrites and implications for aqueous alteration. *Geochim. Cosmochim. Acta* **57**, 2843–2852 (1993). doi:10.1016/0016-7037(93)90393-B

48. T. Nakamura, Yamato 793321 CM chondrite: Dehydrated regolith material of a hydrous asteroid. *Earth Planet. Sci. Lett.* **242**, 26–38 (2006). doi:10.1016/j.epsl.2005.11.040

49. M. K. Weisberg, M. Prinz, R. N. Clayton, T. K. Mayeda, The CR (Renazzo-type) carbonaceous chondrite group and its implications. *Geochim. Cosmochim. Acta* **57**, 1567–1586 (1993). doi:10.1016/0016-7037(93)90013-M

50. M. R. Lee, M. R. Sofe, P. Lindgren, N. A. Starkey, I. A. Franchi, The oxygen isotope evolution of parent body aqueous solutions as recorded by multiple carbonate generations in the Lonewolf Nunataks 94101 CM2 carbonaceous chondrite. *Geochim. Cosmochim. Acta* **121**, 452–466 (2013). doi:10.1016/j.gca.2013.07.010

51. S. M. Richardson, Vein formation in the C1 carbonaceous chondrites. *Meteoritics* **13**, 141–159 (1978). doi:10.1111/j.1945-5100.1978.tb00803.x

52. K. Tomeoka, in *Proceedings of the NIPR Symposum*, K. Yanai, Ed. (National Institute of Polar Research, 1990), vol. 3.

53. C. E. Jilly-Rehak, G. R. Huss, K. Nagashima, 53 Mn– 53 Cr radiometric dating of secondary carbonates in CR chondrites: Timescales for parent body aqueous alteration. *Geochim. Cosmochim. Acta* **201**, 224–244 (2017). doi:10.1016/j.gca.2016.08.033

54. K. Tomeoka, Phyllosilicate veins in a CI meteorite: Evidence for aqueous alteration on the parent body. *Nature* **345**, 138–140 (1990). doi:10.1038/345138a0

55. M. R. Lee, K. Nicholson, Ca-carbonate in the Orgueil (CI) carbonaceous chondrite: Mineralogy, microstructure and implications for parent body history. *Earth Planet. Sci. Lett.* **280**, 268–275 (2009). doi:10.1016/j.epsl.2009.01.038

56. N. P. Hanowski, A. J. Brearley, Iron-rich aureoles in the CM carbonaceous chondrites Murray, Murchison, and Allan Hills 81002: Evidence for *in situ* aqueous alteration. *Meteorit. Planet. Sci.* **35**, 1291–1308 (2000). doi:10.1111/j.1945-5100.2000.tb01517.x

57. M. Gounelle, M. E. Zolensky, A terrestrial origin for sulfate veins in CI1 chondrites. *Meteorit. Planet. Sci.* **36**, 1321–1329 (2001). doi:10.1111/j.1945-5100.2001.tb01827.x

58. P. Lindgren, M. R. Lee, M. Sofe, M. J. Burchell, Microstructure of calcite in the CM2 carbonaceous chondrite LON 94101: Implications for deformation history during and/or after aqueous alteration. *Earth Planet. Sci. Lett.* **306**, 289–298 (2011). doi:10.1016/j.epsl.2011.04.022

59. D. N. DellaGiustina, H. H. Kaplan, A. A. Simon, W. F. Bottke, C. Avdellidou, M. Delbo, R.-L. Ballouz, D. R. Golish, K. J. Walsh, M. Popescu, H. Campins, M. A. Barucci, G. Poggiali, R. T. Daly, L. Le Corre, V. E. Hamilton, N. Porter, E. R. Jawin, T. J. McCoy, H. C. Connolly Jr., J. L. R. Garcia, E. Tatsumi, J. de Leon, J. Licandro, S. Fornasier, M. G. Daly, M. M. Al Asad, L. Philpott, J. Seabrook, O. S. Barnouin, B. E. Clark, M. C. Nolan, E. S. Howell, R. P. Binzel, B. Rizk, D. C. Reuter, D. S. Lauretta, Exogenic Basalt on Asteroid (101955) Bennu. *New Astron.* 10.1038/s41550-020-1195-z (2020). doi:10.1038/s41550-020-1195-z

60. E. A. Cloutis, T. Hiroi, M. J. Gaffey, C. M. O. Alexander, P. Mann, Spectral reflectance properties of carbonaceous chondrites: 1. CI chondrites. *Icarus* **212**, 180–209 (2011). doi:10.1016/j.icarus.2010.12.009

61. M. R. M. Izawa, E. A. Cloutis, T. Rhind, S. A. Mertzman, D. M. Applin, J. M. Stromberg, D. M. Sherman, Spectral reflectance properties of magnetites: Implications for remote sensing. *Icarus* **319**, 525–539 (2019). doi:10.1016/j.icarus.2018.10.002

62. E. A. Cloutis, S. E. Grasby, W. M. Last, R. Léveillé, G. R. Osinski, B. L. Sherriff, Spectral reflectance properties of carbonates from terrestrial analogue environments: Implications for Mars. *Planet. Space Sci.* **58**, 522–537 (2010). doi:10.1016/j.pss.2009.09.002

63. R. N. Clark, Spectral properties of mixtures of montmorillonite and dark carbon grains: Implications for remote sensing minerals containing chemically and physically adsorbed water. *J. Geophys. Res.* **88**, 10635–10644 (1983). doi:10.1029/JB088iB12p10635

64. A. Le Bras, S. Erard, Reflectance spectra of regolith analogs in the mid-infrared: Effects of grain size. *Planet. Space Sci.* **51**, 281–294 (2003). doi:10.1016/S0032-0633(03)00017-5

65. R. J. P. Lyon, W. M. Tuddenham, C. S. Thompson, Quantitative mineralogy in 30 minutes. *Econ. Geol.* **54**, 1047–1055 (1959). doi:10.2113/gsecongeo.54.6.1047

66. A. D. Rogers, O. Aharonson, Mineralogical composition of sands in Meridiani Planum determined from Mars Exploration Rover data and comparison to orbital measurements. *J. Geophys. Res.* **113**, E06S14 (2008). doi:10.1029/2007JE002995

67. R. E. Grimm, H. Y. Mcsween Jr., Water and the thermal evolution of carbonaceous chondrite parent bodies. *Icarus* **82**, 244–280 (1989). doi:10.1016/0019-1035(89)90038-9

68. A. J. Brearley, M. Prinz, CI chondrite-like clasts in the Nilpena polymict ureilite: Implications for aqueous alteration processes in CI chondrites. *Geochim. Cosmochim. Acta* **56**, 1373–1386 (1992). doi:10.1016/0016-7037(92)90068-T

69. M. Zolensky, R. Barrett, L. Browning, Mineralogy and composition of matrix and chondrule rims in carbonaceous chondrites. *Geochim. Cosmochim. Acta* **57**, 3123–3148 (1993). doi:10.1016/0016-7037(93)90298-B

70. E. R. Dufresne, E. Anders, On the chemical evolution of the carbonaceous chondrites. *Geochim. Cosmochim. Acta* **26**, 1085–1114 (1962). doi:10.1016/0016-7037(62)90047-9

71. R. N. Clayton, T. K. Mayeda, Oxygen isotope studies of carbonaceous chondrites. *Geochim. Cosmochim. Acta* **63**, 2089–2104 (1999). doi:10.1016/S0016-7037(99)00090-3

72. P. A. Bland, M. D. Jackson, R. F. Coker, B. A. Cohen, J. B. W. Webber, M. R. Lee, C. M. Duffy, R. J. Chater, M. G. Ardakani, D. S. McPhail, D. W. McComb, G. K. Benedix, Why aqueous alteration in asteroids was isochemical: High porosity≠high permeability. *Earth Planet. Sci. Lett.* **287**, 559–568 (2009). doi:10.1016/j.epsl.2009.09.004

73. E. D. Young, R. D. Ash, P. England, D. Rumble 3rd, Fluid flow in chondritic parent bodies: Deciphering the compositions of planetesimals. *Science* **286**, 1331–1335 (1999). doi:10.1126/science.286.5443.1331 Medline

74. E. D. Young, The hydrology of carbonaceous chondrite parent bodies and the evolution of planet progenitors. *Philos. Trans.- Royal Soc., Math. Phys. Eng. Sci.* **359**, 2095–2110 (2001). doi:10.1098/rsta.2001.0900

75. B. Travis, G. Schubert, Hydrothermal convection in carbonaceous chondrite parent bodies. *Earth Planet. Sci. Lett.* **240**, 234–250 (2005). doi:10.1016/j.epsl.2005.09.008

76. E. D. Young, K. K. Zhang, G. Schubert, Conditions for pore water convection within carbonaceous chondrite parent bodies – implications for planetesimal size and heat production. *Earth Planet. Sci. Lett.* **213**, 249–259 (2003). doi:10.1016/S0012-821X(03)00345-5

77. J. Palguta, G. Schubert, B. J. Travis, Fluid flow and chemical alteration in carbonaceous chondrite parent bodies. *Earth Planet. Sci. Lett.* **296**, 235–243 (2010). doi:10.1016/j.epsl.2010.05.003

78. P. A. Bland, B. J. Travis, Giant convecting mud balls of the early solar system. *Sci. Adv.* **3**, e1602514 (2017). doi:10.1126/sciadv.1602514 Medline

79. Y.-J. Lee, J. W. Morse, Calcite precipitation in synthetic veins: Implications for the time and fluid volume necessary for vein filling. *Chem. Geol.* **156**, 151–170 (1999). doi:10.1016/S0009-2541(98)00183-1

80. M. A. Tyra, J. Farquhar, Y. Guan, L. A. Leshin, An oxygen isotope dichotomy in CM2 chondritic carbonates—A SIMS approach. *Geochim. Cosmochim. Acta* **77**, 383–395 (2012). doi:10.1016/j.gca.2011.10.003

81. L. Wilson, K. Keil, S. J. Love, The internal structures and densities of asteroids. *Meteorit. Planet. Sci.* **34**, 479–483 (1999). doi:10.1111/j.1945-5100.1999.tb01355.x

82. P. Hoppe, D. MacDougall, G. W. Lugmair, High spatial resolution ion microprobe measurements refine chronology of carbonate formation in Orgueil. *Meteorit. Planet. Sci.* **42**, 1309–1320 (2007). doi:10.1111/j.1945-5100.2007.tb00576.x

83. M. Telus, C. M. O. Alexander, E. H. Hauri, J. Wang, Calcite and dolomite formation in the CM parent body: Insight from in situ C and O isotope analyses. *Geochim. Cosmochim. Acta* **260**, 275–291 (2019). doi:10.1016/j.gca.2019.06.012

84. W. Fujiya, N. Sugiura, H. Hotta, K. Ichimura, Y. Sano, Evidence for the late formation of hydrous asteroids from young meteoritic carbonates. *Nat. Commun.* **3**, 627 (2012). doi:10.1038/ncomms1635 Medline

85. C. E. Jilly, G. R. Huss, A. N. Krot, K. Nagashima, Q.-Z. Yin, N. Sugiura, ^{53}Mn-^{53}Cr dating of aqueously formed carbonates in the CM2 lithology of the Sutter's Mill carbonaceous chondrite. *Meteorit. Planet. Sci.* **49**, 2104–2117 (2014). doi:10.1111/maps.12305

86. E. Tonui, M. Zolensky, T. Hiroi, T. Nakamura, M. E. Lipschutz, M.-S. Wang, K. Okudaira, Petrographic, chemical and spectroscopic evidence for thermal metamorphism in carbonaceous chondrites I: CI and CM chondrites. *Geochim. Cosmochim. Acta* **126**, 284–306 (2014). doi:10.1016/j.gca.2013.10.053

87. M. E. Zolensky, N. M. Abreu, M. A. Velbel, A. Rubin, N. Chaumard, T. Noguchi, T. Michikami, in *Primitive Meteorites and Asteroids* (Elsevier, 2018; https://linkinghub.elsevier.com/retrieve/pii/B9780128133255000021), pp. 59–204.

88. T. Nakamura, T. Noguchi, M. E. Zolensky, M. Tanaka, Mineralogy and noble-gas signatures of the carbonate-rich lithology of the Tagish Lake carbonaceous chondrite: Evidence for an accretionary breccia. *Earth Planet. Sci. Lett.* **207**, 83–101 (2003). doi:10.1016/S0012-821X(02)01127-5

89. P. G. Brown, A. R. Hildebrand, M. E. Zolensky, M. Grady, R. N. Clayton, T. K. Mayeda, E. Tagliaferri, R. Spalding, N. D. MacRae, E. L. Hoffman, D. W. Mittlefehldt, J. F. Wacker, J. A. Bird, M. D. Campbell, R. Carpenter, H. Gingerich, M. Glatiotis, E. Greiner, M. J. Mazur, P. J. McCausland, H. Plotkin, T. Rubak Mazur, The fall, recovery, orbit, and composition of the Tagish Lake meteorite: A new type of carbonaceous chondrite. *Science* **290**, 320–325 (2000). doi:10.1126/science.290.5490.320 Medline

90. C. Lantz, R. Brunetto, M. A. Barucci, S. Fornasier, D. Baklouti, J. Bourçois, M. Godard, Ion irradiation of carbonaceous chondrites: A new view of space weathering on primitive asteroids. *Icarus* **285**, 43–57 (2017). doi:10.1016/j.icarus.2016.12.019

91. M. S. Thompson, M. J. Loeffler, R. V. Morris, L. P. Keller, R. Christoffersen, Spectral and chemical effects of simulated space weathering of the Murchison CM2 carbonaceous chondrite. *Icarus* **319**, 499–511 (2019). doi:10.1016/j.icarus.2018.09.022

92. D. S. Lauretta, C. W. Hergenrother, S. R. Chesley, J. M. Leonard, J. Y. Pelgrift, C. D. Adam, M. Al Asad, P. G. Antreasian, R.-L. Ballouz, K. J. Becker, C. A. Bennett, B. J. Bos, W. F. Bottke, M. Brozović, H. Campins, H. C. Connolly Jr., M. G. Daly, A. B. Davis, J. de León, D. N. DellaGiustina, C. Y. Drouet d'Aubigny, J. P. Dworkin, J. P. Emery, D. Farnocchia, D. P. Glavin, D. R. Golish, C. M. Hartzell, R. A. Jacobson, E. R. Jawin, P. Jenniskens, J. N. Kidd Jr., E. J. Lessac-Chenen, J.-Y. Li, G. Libourel, J. Licandro, A. J. Liounis, C. K. Maleszewski, C. Manzoni, B. May, L. K. McCarthy, J. W. McMahon, P. Michel, J. L. Molaro, M. C. Moreau, D. S. Nelson, W. M. Owen Jr., B. Rizk, H. L. Roper, B. Rozitis, E. M. Sahr, D. J. Scheeres, J. A. Seabrook, S. H. Selznick, Y. Takahashi, F. Thuillet, P. Tricarico, D. Vokrouhlický, C. W. V. Wolner, Episodes of particle ejection from the surface of the active asteroid (101955) Bennu. *Science* **366**, eaay3544 (2019). doi:10.1126/science.aay3544 Medline

93. E. B. Bierhaus, B. C. Clark, J. W. Harris, K. S. Payne, R. D. Dubisher, D. W. Wurts, R. A. Hund, R. M. Kuhns, T. M. Linn, J. L. Wood, A. J. May, J. P. Dworkin, E. Beshore, D. S. Lauretta, The OSIRIS-REx Spacecraft and the Touch-and-Go Sample Acquisition Mechanism (TAGSAM). *Space Sci. Rev.* **214**, 107 (2018). doi:10.1007/s11214-018-0521-6

94. E. K. Tonui, M. E. Zolensky, M. E. Lipschutz, M.-S. Wang, T. Nakamura, Yamato 86029: Aqueously altered and thermally metamorphosed CI-like chondrite with unusual textures. *Meteorit. Planet. Sci.* **38**, 269–292 (2003). doi:10.1111/j.1945-5100.2003.tb00264.x

95. W. Nozaki, T. Nakamura, T. Noguchi, Bulk mineralogical changes of hydrous micrometeorites during heating in the upper atmosphere at temperatures below 1000 °C. *Meteorit. Planet. Sci.* **41**, 1095–1114 (2006). doi:10.1111/j.1945-5100.2006.tb00507.x

96. C. M. O. Alexander, G. D. Cody, B. T. De Gregorio, L. R. Nittler, R. M. Stroud, The nature, origin and modification of insoluble organic matter in chondrites, the major source of Earth's C and N. *Chem. Erde Geochem.* **77**, 227–256 (2017). doi:10.1016/j.chemer.2017.01.007 Medline

97. Y. Kebukawa, S. Nakashima, M. E. Zolensky, Kinetics of organic matter degradation in the Murchison meteorite for the evaluation of parent-body temperature history. *Meteorit. Planet. Sci.* **45**, 99–113 (2010). doi:10.1111/j.1945-5100.2009.01008.x

98. H. Y. McSween Jr., J. P. Emery, A. S. Rivkin, M. J. Toplis, J. C. Castillo-Rogez, T. H. Prettyman, M. C. De Sanctis, C. M. Pieters, C. A. Raymond, C. T. Russell, Carbonaceous chondrites as analogs for the composition and alteration of Ceres. *Meteorit. Planet. Sci.* **53**, 1793–1804 (2017). doi:10.1111/maps.12947

99. H. Hiesinger, S. Marchi, N. Schmedemann, P. Schenk, J. H. Pasckert, A. Neesemann, D. P. O'Brien, T. Kneissl, A. I. Ermakov, R. R. Fu, M. T. Bland, A. Nathues, T. Platz, D. A. Williams, R. Jaumann, J. C. Castillo-Rogez, O. Ruesch, B. Schmidt, R. S. Park, F. Preusker, D. L. Buczkowski, C. T. Russell, C. A. Raymond, Cratering on Ceres: Implications for its crust and evolution. *Science* **353**, aaf4759 (2016). doi:10.1126/science.aaf4759 Medline

100. A. Simon, D. Reuter, N. Gorius, A. Lunsford, R. Cosentino, G. Wind, D. Lauretta, the OSIRIS-REx Team, In-Flight Calibration and Performance of the OSIRIS-REx Visible and IR Spectrometer (OVIRS). *Remote Sens.* **10**, 1486 (2018). doi:10.3390/rs10091486

101. Reflectance Experiment Laboratory (RELAB) Spectral Database, (2020), http://www.planetary.brown.edu/relab/

102. R. F. Kokaly, R. N. Clark, G. A. Swayze, K. E. Livo, T. M. Hoefen, N. C. Pearson, R. A. Wise, W. M. Benzel, H. A. Lowers, R. L. Driscoll, A. J. Klein, "USGS Spectral Library Version 7," *Data Series* (Report 1035, Reston, VA, 2017), p. 68.

103. F. A. Kruse, A. B. Lefkoff, J. B. Dietz, Expert system-based mineral mapping in northern death valley, California/Nevada, using the Airborne Visible/Infrared Imaging Spectrometer (AVIRIS). *Remote Sens. Environ.* **44**, 309–336 (1993). doi:10.1016/0034-4257(93)90024-R

104. R. B. Singer, T. B. McCord, Mars - Large scale mixing of bright and dark surface materials and implications for analysis of spectral reflectance, in *Lunar and Planetary Science Conference, 10th, Houston, Tex. March 19-23, 1979, Proceedings* (Pergamon, 1979), vol. 2, pp. 1835–1848.

105. B. Hapke, Bidirectional reflectance spectroscopy: 1. Theory. *J. Geophys. Res. Solid Earth* **86** (B4), 3039–3054 (1981). doi:10.1029/JB086iB04p03039

106. D. N. DellaGiustina, C. A. Bennett, K. Becker, D. R. Golish, L. Le Corre, D. A. Cook, K. L. Edmundson, M. Chojnacki, S. S. Sutton, M. P. Milazzo, B. Carcich, M. C. Nolan, N. Habib, K. N. Burke, T. Becker, P. H. Smith, K. J. Walsh, K. Getzandanner, D. R. Wibben, J. M. Leonard, M. M. Westermann, A. T. Polit, J. N. Kidd Jr., C. W. Hergenrother, W. V. Boynton, J. Backer, S. Sides, J. Mapel, K. Berry, H. Roper, C. Drouet d'Aubigny, B. Rizk, M. K. Crombie, E. K. Kinney-Spano, J. de León, J. L. Rizos, J. Licandro, H. C. Campins, B. E. Clark, H. L. Enos, D. S. Lauretta, Overcoming the Challenges Associated with Image-Based Mapping of Small Bodies in Preparation for the OSIRIS-REx Mission to (101955) Bennu. *Earth Space Sci.* **5**, 929–949 (2018). doi:10.1029/2018EA000382

107. M. G. Daly, O. S. Barnouin, C. Dickinson, J. Seabrook, C. L. Johnson, G. Cunningham, T. Haltigin, D. Gaudreau, C. Brunet, I. Aslam, A. Taylor, E. B. Bierhaus, W. Boynton, M. Nolan, D. S. Lauretta, The OSIRIS-REx Laser Altimeter (OLA) Investigation and Instrument. *Space Sci. Rev.* **212**, 899–924 (2017). doi:10.1007/s11214-017-0375-3

108. M. G. Daly, O. S. Barnouin, J. A. Seabrook, J. Roberts, C. Dickinson, K. J. Walsh, E. R. Jawin, E. E. Palmer, R. Gaskell, J. Weirich, T. Haltigin, D. Gaudreau, C. Brunet, G. Cunningham, P. Michel, Y. Zhang, R.-L. Ballouz, G. Neumann, M. E. Perry, L. Philpott, M. M. Al-Asad, C. L. Johnson, C. D. Adam, J. M. Leonard, J. L. Geeraert, K. Getzandanner, M. C. Nolan, R. T. Daly, E. B. Bierhaus, E. Mazarico, B. Rozitis, A. J. Ryan, D. Dellaguistina, B. Rizk, H. C. M. Susorney, H. L. Enos, D. S. Lauretta, Hemispherical Differences in the Shape and Topography of Asteroid (101955) Bennu. *Sci. Adv.* (2020). 10.1126/sciadv.abd3649

109. M. Kazhdan, H. Hoppe, Screened poisson surface reconstruction. *ACM Trans. Graph.* **32**, 1–13 (2013). doi:10.1145/2487228.2487237

110. Y.-J. Lee, J. W. Morse, D. V. Wiltschko, An experimentally verified model for calcite precipitation in veins. *Chem. Geol.* **130**, 203–215 (1996). doi:10.1016/0009-2541(96)00008-3

111. W. F. Bottke, D. Vokrouhlický, K. J. Walsh, M. Delbo, P. Michel, D. S. Lauretta, H. Campins, H. C. Connolly, D. J. Scheeres, S. R. Chelsey, In search of the source of asteroid (101955) Bennu: Applications of the stochastic YORP model. *Icarus* **247**, 191–217 (2015). doi:10.1016/j.icarus.2014.09.046

112. K. L. Donaldson Hanna, D. L. Schrader, E. A. Cloutis, G. D. Cody, A. J. King, T. J. McCoy, D. M. Applin, J. P. Mann, N. E. Bowles, J. R. Brucato, H. C. Connolly Jr., E. Dotto, L. P. Keller, L. F. Lim, B. E. Clark, V. E. Hamilton, C. Lantz, D. S. Lauretta, S. S. Russell, P. F. Schofield, Spectral characterization of analog samples in anticipation of OSIRIS-REx's arrival at Bennu: A blind test study. *Icarus* **319**, 701–723 (2019). doi:10.1016/j.icarus.2018.10.018